



Self-adapting PI controller for grid-connected DFIG wind turbines based on recurrent neural network optimization control under unbalanced grid faults

Elmostafa Chetouani^{*}, Youssef Errami, Abdellatif Obbadi, Smail Sahnoun

Laboratory: Electronics, Instrumentation and Energy – Team: Exploitation and Processing of Renewable Energy – Department of Physics – Faculty of Sciences, University of Chouaib Doukkali, El Jadida, Morocco

ARTICLE INFO

Keywords:

DFIG
Grid faults
MPPT
PI controller
Recurrent neural network
and Wind power plant system

ABSTRACT

This paper suggests the Hidden Layer Recurrent Neural Network (HLRNN) for controlling a wind power generation system based on a dual-fed induction generator. The generator's stator is connected directly to the electrical grid, while the rotor is linked through bidirectional converters. A PI controller-based Indirect Vector Control (IVC) scheme has been established to pilot the system. The PI regulator allows linear systems to perform well, but when subjected to physical variation conditions, the system's response becomes unstable, making the PI controller insufficient. This paper aims to ensure the PI controller gains self-adaptation regardless of the severity of the circumstances. The effectiveness of the proposed control is demonstrated by taking into account critical conditions such as wind speed changes, generator parameter variations, and asymmetrical faults in the grid. Furthermore, it is confirmed by the enhanced performance and the reduced oscillations during a voltage dip. The simulation results, achieved using MATLAB/Simulink, demonstrate that the response time is reduced to 1.8 (m s), the static error is minimized to 0.16%, and the overshoot is improved to 0.24% when compared to the IVC based on the PI controller and some existing neural network schemes.

1. Introduction

On account of the growth of the population and home automation devices, there was a significant increase in electrical energy demand. A great quantity of energy is based on fossil fuel energy. So, many challenges, such as environmental pollution and the significance of the increase in the cost of fossil fuels, are due to several causes, such as war, political reasons, etc. For these reasons, renewable energy, especially wind energy, has been considered an alternative solution because it is environmentally friendly and independent of the fluctuations in prices of fossil fuel energy and inexhaustible energy [1,2]. In addition to these benefits, current and future technological advancements encourage countries to invest in this field.

The dual-fed induction generator is the most commonly utilized machine in wind energy systems because of its many advantages [3,4]. Therefore, the bidirectional converters transfer about 25%–30% of the rated power, and the rest of the power is transmitted directly to the electrical grid, which minimizes cost and power losses and reduces the size of the converters [5,6]. The stator of the generator is connected directly to the grid. However, the rotor is branched to the electric power via AC/DC/AC Converters, including the Grid Side Converter (GSC) and

the Rotor Side Converter (RSC) [7], as depicted in Fig 1. The converters use IGBT switches controlled by using Sinusoidal Pulse Width Modulation (SPWM) to reduce the harmonics that exist in the grid-injected currents. The RSC governs the stator power produced by the generator by managing the speed of rotation and rotor currents. The GSC, on the other hand, keeps the DC bus voltage constant [8]. The DFIG has a complex system of electrical and mechanical equations with strongly coupled flux and electromagnetic torque. As a result, active and reactive power are implicitly coupled [5]. Besides, the accurate control of the RSC and GSC contributes to the grid-connected DFIG's stability. The vector control (VC) scheme is a widely used and researched method for independently controlling the active and reactive power of a wound rotor induction generator [9]. This method employs Park Transformation to solve the complexity of the equation system and the orientation of the rotor/stator flux or the voltage according to the component "d" or "q" axis of the rotating d-q referee, allowing each quantity to be managed independently without affecting the other. M. Bouderbala et al. [10] have compared and analyzed the two vector control variants, Direct and Indirect Field Oriented Control (DFOC and IFOC). The first performs the voltages directly, ignoring the coupling terms between the two axes, and employs two PI regulators to pilot the

^{*} Corresponding author.

E-mail address: chetouani.m@ucd.ac.ma (E. Chetouani).

<https://doi.org/10.1016/j.epsr.2022.108829>

Received 28 July 2022; Received in revised form 7 September 2022; Accepted 21 September 2022

Available online 27 September 2022

0378-7796/© 2022 Elsevier B.V. All rights reserved.

powers. The second considers the linkage terms and compensates them by using PI controllers. The latter variant is classified into two types. One controls the closed-loop current and the open-loop powers, while the other pilots the active/reactive power and the current in the closed-loop [11,12]. Besides, the vector control scheme is utilized to establish grid-side converter control by regulating grid currents and DC link voltage [11]. As is known, VC control, with its different variants based on the PI controller, is the most commonly utilized control in the industrial process of the alternative motors because it has the characteristics of simplicity and reveals satisfactory performance in terms of precision, stability, and response time. Therefore, it has two inherent problems [12]. The first is that the PI Controller gain calculation is dependent on the system settings. As a result, defective settings or any change in the regulator parameters as a result of temperature elevation, machine device damage, grid fault, etc., can result in oscillating dynamic response and even system instability or negatively affect system performance [13,14]. The second issue is a lack of self-adaptability in response to external disturbances [15]. Recently, many methods have been proposed to deal with these vector control limitations. The most popular methodologies used to manage wind turbine systems are Fuzzy Logic Control (FLC) and Neural Network (NN). NN systems imitate the function of the human central nervous system, while FLC systems rely on the operator’s qualitative knowledge of the system. The first demonstrates the benefits of being robust, fast, simple, and describing systems as numeric and symbolic associations. However, because the FLC is not always accurate, the results are perceived based on assumptions, and may not be broadly accepted. Furthermore, due to the difficulty of precisely defining the fuzzy laws and membership functions and testing a fuzzy knowledge-based system, extensive testing with hardware is required. Furthermore, fuzzy logic-based systems lack the capacity of neural networks and machine learning-type model recognition [16]. The second method has several advantages, including a relatively simple training algorithm, the capacity to surpass other models in the presence of high-quality information and data, the ability to estimate any function regardless of its linearity, fast learning abilities from examples, parallel processing, the ability to solve nonlinear problems, and fault tolerance [17,18]. However, it has some significant drawbacks such as hardware dependence, unexplained network functioning, assurance of proper network structure, difficulty in showing the problem to the network and the network’s duration is unknown [16]. There are two main NN architectures: the Feed-Forward and the Recurrent Neural Networks

(FNNs and RNNs). Most researchers employ feed-forward (FNN) models in conjunction with the back-propagation learning algorithm to resolve different dynamical problems. Nevertheless, the FNN is fixed mapping and does not provide dynamical mapping without using tapping delays [19]. The recurrent neural network, on the other hand, is a widely used model with significant capabilities not found in FNN, such as attractor dynamics and the capacity to hold information for future needs. Besides, their capacity to handle time-varying input or output via their own neural natural temporal process is particularly intriguing [19]. As a result, the RNN is a dynamic mapping that is best placed for dynamical systems than the FNN. More importantly, RNNs are classified into two types: Completely and Partially Recurrent Neural Networks (CRNNs and PRNNs). The learnable weights are used to link the hidden layer to the output layer in the first one. This engenders a complex model, leading to an extremely difficult learning process. However, in the second, there is only a local feedback linkage rather than a global one. This leads to a simpler network architecture with a memory characteristic and thus a less complex training process [20]. The hidden layer recurrent neural network structure (HLRNN), commonly called the Diagonal Recurrent Neural Network (DRNN), is a type of PRNN. Therefore, the only recurrent connections permitted in a HLRNN are self-recurrent connections in the hidden layer, in which the recurrence connections are considered to include a waiting time. When the self-recurrent interconnections are removed, the structure transforms into a feed-forward network. Although compared to feed-forward and fully recurrent NN topologies, the HLRNN uses fewer neurons, is easier to implement in real-time systems, and provides faster results [21].

A wound rotor induction generator produces power at a low cost, allowing for competitive prices and more power output ability. Nevertheless, the generator systems are very sensitive to grid problems and subject to unstable operation conditions. Consequently, these issues led to the disconnection of the generator from the grid. In the power grid utility, a short circuit between phases, known as a Voltage Dip (VD), can destabilize and produce high oscillations in the produced power, raise the DC-link voltage, and increase the stator and rotor currents [22]. As a result, a conventional PI controller cannot reduce the ripples and cannot eliminate the steady-state error of the alternative oscillations [23]. Another potential issue that could destabilize the electrical grid is that when a crowbar system protection is activated. So, the DFIG can act like a squirrel-cage induction asynchronous generator due to short-circuited rotor windings [24]. Besides, a squirrel-cage induction asynchronous

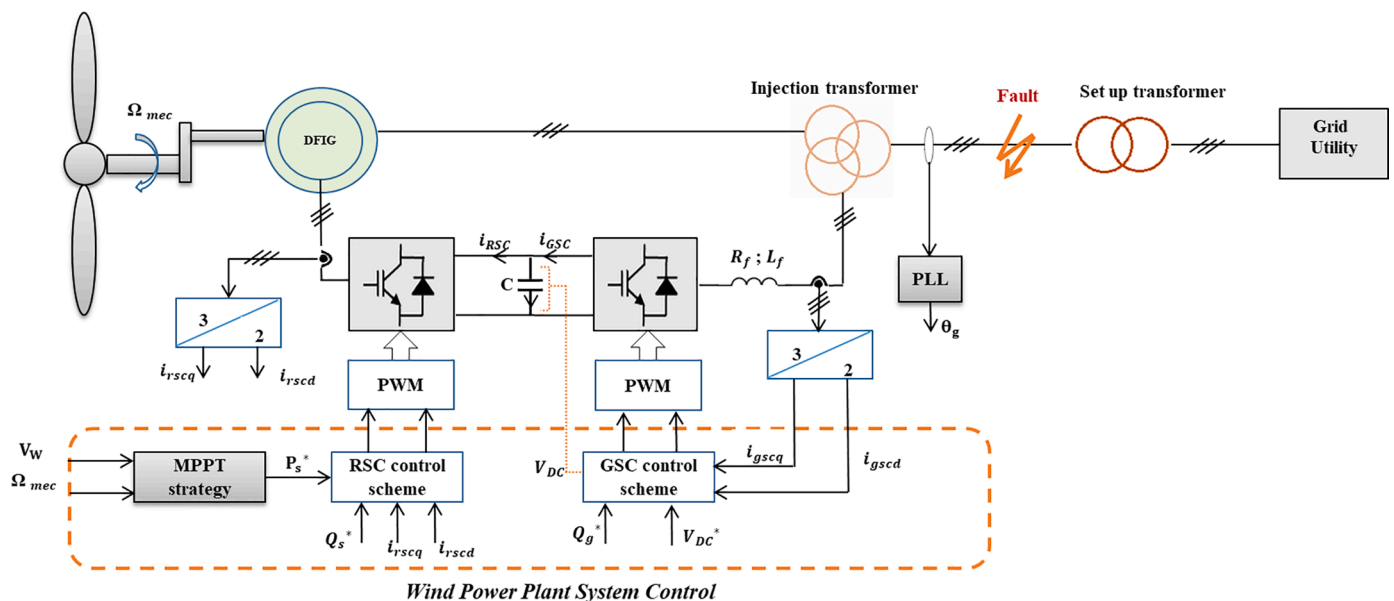


Fig 1. Wind energy conversion based on DFIG configuration.

generator absorbs reactive power from the grid, resulting in a voltage drop in the transmission line [25]. More recently, researchers have expressed an interest in testing and validating control approaches while the system is connected to an electrical network. Besides, many methods can be used to dampen the oscillations observed in the generated power. Authors in [24] have proposed a hybrid control based on Fuzzy Logic Control and a PI controller to regulate Fault Ride Through with a crowbar to mitigate the oscillations and ensure system protection. Furthermore, in all investigated scenarios, D. Çelik [26] has used a shunt active power filter to keep the THD value of the source current within the predefined limits. In addition, the author has proposed the Lyapunov with a proportional integral algorithm with anti-windup to control and reduce the DC-link voltage oscillations. Besides, in [27] the hybrid control based on the Sliding Mode Control (SMC) and the adaptive linear neuron (ADALINE) proportional resonant (PR) is proposed for controlling the grid interfaced Vienna rectifier. The SMC was used to regulate the DC-link voltage, and ADALINE-PR was proposed to control the source current. The simulation results show that the ADALINE-PR presents a fast dynamic response, very low THD, and very low oscillation in the generated power and DC-link voltage. The system's ability to generate power in the event of grid faults, which are frequently caused by short circuits, is also gaining attention [28,29]. Grid failures might be classed as symmetrical or asymmetrical. The symmetrical malfunction affects all phases of the system while keeping it balanced. The symmetrical fault is a three-phase fault. Unsymmetrical or asymmetrical faults are the names given to the other three fault types (One Line-to-Ground (L2G), Line-to-Line (L2L), and Double-Line-to-Ground (LL2G)) [30,31]. K. Tamvada et al. (2018) [30] have utilized the vector control strategy to pilot the system and studied the behavior of the DFIG under symmetrical and unsymmetrical grid fault conditions. In this paper, the proposed control is tested in the case of an asymmetrical fault. Furthermore, H. Elaimani et al. (2020) [32] employed Sliding Mode Control to govern the RSC and GSC and compared the GSC controlled by the PI Controller and SMC when exposed to a voltage dip.

Because of the fluctuating and intermittent nature of the wind speed profile, the Maximum Power Point Tracking (MPPT) algorithm should be designed and improved to track the peak power produced by wind turbines from wind energy [7]. Thus, the maximum power value is determined by the nature and characteristics of each rotor blade and the wind's fluctuating velocity [33]. Several methodologies have been proposed to carry out this algorithm. The MPPT with Optimal Tip Speed Ratio (OPTSR) and the MPPT with Power Signal Feedback (PSF) are two techniques that require measurement of the wind power speed via a sensor. However, the wind velocity is estimated without sensors in the MPPT with Optimal Torque Control (OTC) and the MPPT with Perturbation and Observation (P & O) algorithms [34]. Recently, intelligent methodologies, such as neural networks and fuzzy logic, have been suggested for developing MPPT algorithms. More information is available in the review established by H.H. Mousa et al. [35]. In addition, [36] have conducted a comparative study of these techniques and the perturbation and observation algorithm. The authors have demonstrated that neural networks provide a faster response time than fuzzy logic and (P & O), respectively. Besides, A. A. Chhipa et al. [37] have suggested a hybrid of these two methods called the Adaptive Neuro-Fuzzy Inference System to establish the MPPT algorithm. In this manuscript, the MPPT using the OPTSR based on the PI controller was chosen and developed because it is efficient, less complex, and has a faster convergence speed with no oscillation, as indicated by [34,35]. Besides, the PI Controller gains are self-tuning using the HLRNN algorithm in order to adapt the controller to any change in the wind speed and get a more rapid response.

This article suggests and establishes the hidden layer recurrent neural network for adapting the parameters of the PI controllers. The HLRNN method provides better response time, minimizes overshoot, and maintains adequate tracking of the reference under severe conditions such as changes in wind speed, generator parameter variation, and

grid voltage dip caused by asymmetrical phase fault. The following points highlight the study's contributions:

- The MPPT with OPTSR is combined with HLRNN to gain faster convergence.
- The simulation results are compared to those obtained using conventional PI controllers and with some existing work.
- The performance of the suggested method is evaluated in terms of power convergence and DC bus voltage.
- Finally, the efficiency of the proposed approach control system is demonstrated adopting Matlab/Simulink simulation with a 5 MW DFIG wind turbine under severe conditions such as generator parameter variations and asymmetrical grid faults.

The remainder of the paper is arranged as follows: Section 2 focuses on the most recent articles in Neural Networks used for WECS based on DFIG Section 3 investigates the mathematical models of wind power plant systems as well as the indirect vector control for wind chains. Section 4 examines the hidden layer recurrent neural network for tuning the different PI Controllers. Section 5 examines and contrasts the outcomes of the two studied strategies, as well as evaluates the suggested control in a variety of severe scenarios such as changeable wind speed, generator parameter modification, and grid faults. Finally, section 6 presents the conclusions.

2. Report on the most recent papers on Neural Networks applied for WECS based on DFIG

Neural Networks with their different architectures, whether single or multi-layer, and various neural learning schemes have been developed and utilized in various applications. Also, NNs have been used in the modeling, identification, optimization, predicting, and control of complex and non-linear systems [18]. Moreover, NNs are widely used in wind turbine systems for many issues such as determining the optimal value of the PI Controllers, replacing the PI or PID Controllers (Proportional-Integral-Derivative), as well as identifying the parameters of adaptive control (Nonlinear Backstepping Control, Sliding Mode Control, etc.) and estimating the uncertainties. S. Mahfoud et al. (2022) [38] have suggested an Intelligent Direct Torque Control (DTC) by replacing the speed controller, switching tables, and hysteresis comparators with Neural Network to improve the inconvenient of the classical DTC, that is the presence of the ripples, especially in low speed of the generator as well as the improvement of the THD of the rotor and stator currents. The authors trained the neural network method employing the feed forward back-propagation approach to reduce the mean square error, which was chosen as the cost function. The number of hidden layer neurons is determined through trial and error until the required performance is attained. S. Labdai et al. (2021) [39] have proposed an artificial neural network to approximate uncertainties and reject external disturbances for an adaptive control based on the Lyapunov function. The authors have compared the proposed method to Sliding Mode Control and Field Oriented Vector Control. The effectiveness and robustness of the proposed control against the uncertainties have been demonstrated. The authors employed a neural network layout with a single hidden layer of 10 neurons. The output layer is activated using a sigmoid function. In [40], a Deep Learning Neural Network (DLNN) model with its tuned weights using an optimization technique has been used to determine the gain values of the PID controller. A multi-layer feed forward network with numerous hidden layers is the DLNN topology. There are two hidden layers, each with four neurons. The authors classified the DLNN method training into two stages: pre-training, which is based on unsupervised learning techniques, and fine-tuning, which is based on the back propagation neural network training algorithm. A gray artificial bee colony algorithm is used to tune weights. A sigmoid function is used to enable the output layer. In [41], the authors have proposed the feed-forward neural network (FFNN) architecture to optimize and

control the DFIG The authors have compared three kinds of these structures, which are probabilistic FFNN, multi-layer perceptron FFNN and radial basic function FFNN, with the conventional controllers. The simulation results validate the superiority of the RBFNN over the other types. The authors employed one hidden layer with 25 neurons, which has been shown to improve performance. The linear transfer function is utilized to trigger neuron output. The settling time for the active power response is 1.33 (s) with a 38% overshoot for a step input. J. Tavoosi et al. (2022) [42] have replaced the PI controllers in the outer loop with a combination of the Recurrent Neural Network and Fuzzy Logic Type-II (RT2FNN) to control the power of a grid-connected. However, the current in the inner loop is controlled using PI Controller. This proposed control is designed based on the concept of the Radial Basis Function Network. The multi-layer structure with a self-recurrent hidden layer was used by the authors. Furthermore, the weights are expected to be Gaussian Type-II sets. A comparison study between the proposed approaches is performed. The results show that the active power response time is 1.7 (s) with a 0.32% overshoot. Furthermore, B. Boudjellal et al. (2020) [43] have used an artificial neural network to regulate independently the stator powers in open-loop instead of the two PI controllers. A (2–7–1) structure Multilayer Perceptron networks was utilized. The authors have adopted for the input, hidden, and output layer the tan-sigmoid, the log-sigmoid, the linear activation function, respectively. The simulations results reveal that the response time of the active power is 0.028 (s). In addition, H. Benbouhenni et al. (2021) [12] have proposed a Neural Direct Vector Control (NDVC) based on feed forward neural networks with the Levenberg–Marquardt algorithm. The authors have compared the proposed control with the standard Direct Vector Control (DVC). The simulation results show that the NDVC outperforms the DVC with a response time of 1.78 (m s).

By analyzing this report of the previous works, we can observe that the response time needs to be improved due to the intermittent nature of the wind profile. In this context, we apply the HLRNN control to the whole wind energy system. This paper presents a completed and detailed study for academic and industrial research in the field.

3. Wind power plant system modeling and vector control

3.1. Wind turbine modeling

Wind turbines generate electricity by transforming kinetic energy in the wind into rotational kinetic energy in the turbine. Therefore, the mechanical power (P_{Tu-mec}) is stated as [44,45]:

$$P_{Tu-mec} = 0.5 \cdot C_{p-Tu}(\beta_{-Tu}, \lambda_{-Tu}) \cdot \rho \cdot \pi \cdot R^2 \cdot V_{wind}^3 \quad (1)$$

The mechanical torque C_{Tu-mec} is given by:

$$C_{Tu-mec} = \frac{P_{Tu-mec}}{\Omega_{Tu-mec}} \quad (2)$$

Where V_{wind} is the wind energy speed (in m/s), ρ denotes the air mass per unit volume (in kg/m^3), R is the turbine radius (in m), Ω_{Tu-mec} is the turbine speed (in rad/s), and C_{p-Tu} denotes the turbine's performance coefficient. C_{p-Tu} could be expressed as [3,18]:

$$C_{p-Tu}(\beta_{-Tu}, \lambda_{-Tu}) = [0.5 - 0.0167 \cdot (\beta_{-Tu} - 2)] \cdot \sin\left(\frac{\pi(\lambda_{-Tu} + 0.1)}{18.5 - 0.3 \cdot (\beta_{-Tu} - 2)}\right) - 0.00184 \cdot (\lambda_{-Tu} - 3) \cdot (\beta_{-Tu} - 2) \quad (3)$$

The power coefficient is not a fixed rate and changes with the turbine's tip speed ratio (TSR). The TSR is formulated as follows:

$$\lambda_{-Tu} = \frac{R \cdot \Omega_{Tu-mec}}{V_{wind}} \quad (4)$$

3.2. Gearbox modeling

The mechanical equation of the system is shown in Eq. (5), with the total mechanical dynamics being taken back to the rotor blade shaft [44]:

$$J_{-tot} \cdot \frac{d\Omega_{rot-mec}}{dt} + f_r \cdot \Omega_{rot-mec} = C_g - C_{Tem} \quad (5)$$

With

$$C_g = \frac{C_{Tu-mec}}{G_{Box}}; G_{Box} = \frac{\Omega_{rot-mec}}{\Omega_{Tu-mec}} \quad (6)$$

Where J_{-tot} is the total inertia of the wind chain, C_{Tu-mec} is the turbine torque, C_{Tem} is the generator's electro-magnetic torque, f_r is the total viscous coefficient of friction, $\Omega_{rot-mec}$ represents the rotational speed at the rotor axis of the gearbox (rad/s) and G_{Box} denotes the gearbox's multiplier factor.

3.3. Electrical equation of the DFIG modeling

It is advantageous to move towards a more appropriate reference frame to obtain a simpler model of the generator. The Park transformation allows the three-phase frame to be transferred to a rotating reference frame (dq-reference frame). So, stator and rotor voltages equations are expressed as follows [40,46]:

$$\begin{aligned} V_{gr-d} &= R_{sta} \cdot i_{sta-d} + \frac{d\varphi_{sta-d}}{dt} - \omega_{gr} \cdot \varphi_{sta-q} \\ V_{gr-q} &= R_{sta} \cdot i_{sta-q} + \frac{d\varphi_{sta-q}}{dt} + \omega_{gr} \cdot \varphi_{sta-d} \\ V_{rot-d} &= R_{rot} \cdot i_{rot-d} + \frac{d\varphi_{rot-d}}{dt} - \omega_{rot} \cdot \varphi_{rot-q} \\ V_{rot-q} &= R_{rot} \cdot i_{rot-q} + \frac{d\varphi_{rot-q}}{dt} + \omega_{rot} \cdot \varphi_{rot-d} \end{aligned} \quad (7)$$

Where V_{rot} and V_{gr} indicate the rotor and grid voltage; i_{sta} and i_{rot} describe the currents; φ_{sta} and φ_{rot} represent the flux; R_{sta} and R_{rot} identify the resistors of windings; ω_{gr} and ω_{rot} are the angular pulses; L_{sta} and L_{rot} denote the inductances; L_m represents the Mutual inductance. The rotor and stator are designated by the characters "rot" and "sta," respectively. The electro-magnetic torque is given below [43]:

$$C_{Tem} = - p_{pole} \cdot \frac{L_m}{L_{sta}} (i_{rot-q} \cdot \varphi_{sta-d} - i_{rot-d} \cdot \varphi_{sta-q}) \quad (8)$$

The number of DFIG pole pairs is indicated p_{pole} . The stator active and reactive powers are written as follows [10]:

$$P_s = V_{gr-d} \cdot i_{sta-d} + V_{gr-q} \cdot i_{sta-q} \quad (9)$$

$$Q_s = V_{gr-q} \cdot i_{sta-d} - V_{gr-d} \cdot i_{sta-q} \quad (10)$$

3.4. Maximization of the generated power

Under normal wind turbine operation, the MPPT approach is established to maximize the available energy in the wind. The MPPT method is designed, with mechanical speed control. This methodology involves maintaining the generator speed stable at its reference, which is achieved when the C_p is optimum. The electro-magnetic torque (C_{Tem}) developed by the DFIG is equivalent to the reference value applied by the control [47,48]:

$$C_{Tem} = C_{Tem-opt} \quad (11)$$

The optimized electro-magnetic torque $C_{Tem-opt}$ for achieving optimum rotation velocity is given as follows:

$$C_{Tem-opt} = \left[T_{p-mppt} + T_{i-mppt} \cdot \frac{1}{S} \right] \cdot [\Omega_{rot-mec-opt} - \Omega_{rot-mec}] \quad (12)$$

Where T_{p_mppt} and T_{i_mppt} are the MPPT regulator gains. The optimal mechanical speed ($\Omega_{rot_mec_opt}$) is [47]:

$$\Omega_{rot_mec_opt} = G_{Box} \cdot \Omega_{Tu_mec_opt}$$

With

$$\Omega_{Tu_mec_opt} = \frac{V_{wind} \cdot \lambda_{-Tu}}{R} \quad (13)$$

Calculation of MPPT regulator gains. The pole compensation technique was utilized to compute the PI regulator parameters. In [48], more information on the PI gains calculation approach is provided. So, the system's time constant (T_{sys}) is:

$$T_{sys} = \frac{J_{tot}}{f_r} \quad (14)$$

The gains of the MPPT regulator are determined as:

$$T_{impppt} = \frac{1}{\tau \cdot f_r} ; \quad T_{p_mppt} = \frac{-T_{i_mppt} \cdot J_{tot}}{f_r}$$

With

$$\tau = \frac{T_{sys}}{1000} \quad (15)$$

3.5. Indirect field oriented control methodology

3.5.1. Rotor side converter control

The indirect vector control is used to regulate the powers of the generator separately and to address the system's coupling problem. The powers are piloted in the open loop, while the closed loop is utilized to govern rotor currents. Stator flux is assumed to be constant and is oriented with the d-axis. Because the stator windings resistor is eliminated, the voltage expression might be modified as follows [10]:

$$\begin{aligned} \varphi_{sta_d} &= \varphi_{sta} ; & \varphi_{sta_q} &= 0 \\ V_{gr_d} &= 0 ; & V_{gr_q} &= V_{gr} = \omega_s \cdot \varphi_{sta} \end{aligned} \quad (16)$$

The rotor voltage expressions can be written using the Laplace Transform as [10]:

$$V_{rot_d} = \left[R_{rot} + \left(L_{rot} - \frac{L_m^2}{L_{sta}} \right) \cdot s \right] i_{rot_d} - g \cdot \omega_{gr} \left(L_{rot} - \frac{L_m^2}{L_{sta}} \right) i_{rot_q} \quad (17)$$

$$V_{rot_q} = \left[R_{rot} + \left(L_{rot} - \frac{L_m^2}{L_{sta}} \right) \cdot s \right] i_{rot_q} + g \cdot \omega_{gr} \left(L_{rot} - \frac{L_m^2}{L_{sta}} \right) i_{rot_d} + g \cdot \frac{V_{gr} \cdot L_m}{L_{sta}} \quad (18)$$

Where g is the DFIG's slip.

The rotor currents equations are conducted using Eqs. (17) and (18), as follows:

$$i_{rot_d} = \left[V_{rot_d} + g \cdot \omega_{gr} \left(L_{rot} - \frac{L_m^2}{L_{sta}} \right) i_{rot_q} \right] / \left[R_{rot} + \left(L_{rot} - \frac{L_m^2}{L_{sta}} \right) \cdot s \right] \quad (19)$$

$$i_{rot_q} = \left[V_{rot_q} - g \cdot \omega_{gr} \left(L_{rot} - \frac{L_m^2}{L_{sta}} \right) i_{rot_d} - g \cdot \frac{V_{gr} \cdot L_m}{L_{sta}} \right] / \left[R_{rot} + \left(L_{rot} - \frac{L_m^2}{L_{sta}} \right) \cdot s \right] \quad (20)$$

The following are the rotor current references [10]:

$$i_{rot_q}^* = -\frac{L_{sta}}{L_m \cdot V_{gr}} \cdot P_s^* \quad (21)$$

$$i_{rot_d}^* = -\frac{L_{sta}}{L_m \cdot V_{gr}} \cdot \left(Q_s^* - \frac{V_{gr}^2}{\omega_{gr} \cdot L_{sta}} \right) \quad (22)$$

The voltage references can be defined using Eqs. (17) and (18), as follows:

$$V_{rot_q}^* = \left[i_{rot_q}^* - i_{rot_q} \right] \cdot \left[T_{p_rsc1} + T_{i_rsc1} \cdot \frac{1}{s} \right] + e_{r_d} + V_{s'} \quad (23)$$

$$V_{rot_d}^* = \left[i_{rot_d}^* - i_{rot_d} \right] \cdot \left[T_{p_rsc2} + T_{i_rsc2} \cdot \frac{1}{s} \right] + e_{r_q} \quad (24)$$

Where

$$e_{r_d} = g \cdot \omega_{gr} \left(L_{rot} - \frac{L_m^2}{L_{sta}} \right) \cdot i_{rot_d}$$

$$e_{r_q} = g \cdot \omega_{gr} \left(L_{rot} - \frac{L_m^2}{L_{sta}} \right) \cdot i_{rot_q}$$

$$V_{s'} = g \cdot \frac{V_{gr} \cdot L_m}{L_{sta}} \quad (25)$$

3.5.2. Determination of RSC controller gains

The pole compensation approach is utilized to calculate the PI coefficients (T_{p_rsc} , T_{i_rsc}). The system's time constant is [48]:

$$T_s = \left(L_{rot} - \frac{L_m^2}{L_{sta}} \right) / R_{rot} \quad (26)$$

Therefore, the expressions of PI coefficients (T_{p_rsc} , T_{i_rsc}) are computed as follows [48]:

$$T_{p_rsc} = \frac{1}{T_{rsc}} \cdot \left(L_{rot} - \frac{L_m^2}{L_{sta}} \right)$$

$$T_{i_rsc} = \frac{T_{p_rsc} \cdot R_{rot}}{\left(L_{rot} - \frac{L_m^2}{L_{sta}} \right)}$$

With

$$T_{rsc} = \frac{T_s}{100} \quad (27)$$

3.5.3. Grid side converter control

The GSC regulates the DC-link voltage and reactive power transferred with the electrical network. The grid voltage is regarded oriented to the q-axis and is obtained using the Park transformation to develop the GSC control methodology. To estimate the angle of transformation, the Phase-Locked Loop (PLL) strategy is utilized. More details about the development of the PLL approach are provided in [48]. Thus, grid voltages can be stated as follows:

$$V_{gr_d} = 0 ; \quad V_{gr_q} = V_{gr} \quad (28)$$

The voltages and powers can be reduced to the following [49]:

$$V_{gsc_d} = -[R_f + L_f \cdot s] \cdot i_{gsc_d} + \omega_{gr} \cdot L_f \cdot i_{gsc_q} \quad (29)$$

$$V_{gsc_q} = -[R_f + L_f \cdot s] \cdot i_{gsc_q} - \omega_{gr} \cdot L_f \cdot i_{gsc_d} + V_{gr} \quad (30)$$

$$P_g = V_{gr} \cdot i_{gsc_q} \quad (31)$$

$$Q_g = V_{gr} \cdot i_{gsc_d} \quad (32)$$

The connection between converters powers can be represented as follows [45,49]:

$$V_{DC} \cdot i_C = P_{g_gsc} - P_{g_rsc} \quad (33)$$

The power of the grid-side converter is calculated as below:

$$P_g = P_{g_gsc} = V_{DC} \cdot i_C + P_{g_rsc} \quad (34)$$

Where P_{g_RSC} is the power of the RSC, which is described as:

$$P_{g_rsc} = V_{DC} \cdot i_{rsc} \quad (35)$$

The DC-link power reference (P_{dc}^*) is written as follows:

$$P_{dc}^* = V_{DC} i_c^* \quad (36)$$

The references of the grid currents are computed from Eqs. (31), (32), (33), and (34) as follows:

$$i_{gsc-q}^* = \frac{1}{V_{gr}} \cdot (V_{DC}^* i_c^* + P_{g-rsc}) ; \quad i_{gsc-d}^* = \frac{Q_g^*}{V_{gr}} \quad (37)$$

To have a unit power factor, it is supposed that the reference of reactive power is null. As a result, we apply a zero direct current grid reference ($i_{gsc-d}^* = 0$). The voltage references are as follows [50]:

$$V_{gr-d}^* = [i_{gsc-d}^* - i_{gsc-d}] \cdot [T_{p-gsc2} + T_{i-gsc2} \cdot \frac{1}{s}] + e_{gsc-q} \quad (38)$$

$$V_{gr-q}^* = [i_{gsc-q}^* - i_{gsc-q}] \cdot [T_{p-gsc1} + T_{i-gsc1} \cdot \frac{1}{s}] - e_{gsc-d} + V_{gr} \quad (39)$$

Where

$$e_{gsc-q} = \omega_g L_f i_{gsc-q} ; \quad e_{gsc-d} = \omega_g L_f i_{gsc-d} \quad (40)$$

The following are the expressions for grid currents [3]:

$$i_{gsc-q} = \frac{1}{[R_f + L_f \cdot s]} \cdot (V_{gr-q}^* - \omega_{gr} L_f i_{gsc-d} - V_{DC} S_d) \quad (41)$$

$$i_{gsc-d} = \frac{1}{[R_f + L_f \cdot s]} \cdot (V_{gr-d}^* + \omega_{gr} L_f i_{gsc-q} - V_{DC} S_d) \quad (42)$$

Where S_d and S_q are the Park transformation switching states. The PI_{DC} regulator is used to control the DC-link voltage at the reference. As a result, the regulator settings are as follows:

$$\begin{aligned} T_{p-DC} &= 2 \cdot \xi \cdot \omega_c \\ T_{i-DC} &= \omega_c^2 \cdot c ; \quad \text{Where } \xi \text{ is the damping coefficient} \end{aligned} \quad (43)$$

The currents i_{gsc-q} and i_{gsc-d} , flowing through the RL filter, are controlled by a PI_{GSC} regulator utilized in the inner loop. Taking the managed system's time constant (T_{gsc}) into account, the PI_{GSC} parameters are [42]:

$$T_{p-gsc1,2} = \frac{L_f}{T_{gsc}} ; \quad T_{i-gsc1,2} = \frac{R_f}{T_{gsc}} \quad (44)$$

4. Wind turbine system-based dfig controlled by recurrent neural networks

4.1. Problem description

The stator powers, which are controlled indirectly through the d-q component rotor currents in closed-loop as described in Eqs. (21, 22), DC-Link voltage, as shown in Eq. (37), and grid currents, as demonstrated in Eqs. (41, 42), are the quantities to control for the investigated system. To operate the system, a conventional PI Controller with simple characteristics is typically used. Unfortunately, this controller confronts difficulties such as gain dependency on system parameters, limited robustness, and poor performance. Hidden layer recurrent neural network approach is developed for self-tuning the gains of the PI regulators and guaranteeing the self-independence of the generator settings to improve the dynamic performance of the variable power plant system based on DFIG. The PI regulator has two gains: one that takes into account the present error (Proportional) and one that indicates the accumulation of past errors (Integral). Each of these errors is weighted by a scalar value (T_p , T_i) and the sum is calculated. This amount is then fed into the control system. The control concept of a standard PI regulator is then as follows:

$$u(t) = T_{Pi} \cdot e(t) + T_{Pi} \cdot \int_0^t e(t) dt \quad (45)$$

4.2. Self-Adapting PI controller gains based on hidden layer recurrent neural network

4.2.1. HLRNN structure

A hidden layer recurrent neural network is a derivative of a fully associated recurrent neural network with one hidden layer made up of self-recurrent neurons. This method was chosen to automatically update the PI regulator gains because of its simplicity and effectiveness, lower reaction time, and capacity to have a similar dynamic mapping response as other forms of recurrent neural networks [44]. The HLRNN structure depicted in Fig 2 is made up of three layers. Three neurons comprise the input layer: the regulator delayed neuron's output command, the actual output neuron, and the bias. With adjustable weights represented by the weight vector (W_i) the input layer is linked to the hidden layer. However, several neurons make up the hidden layer. The latter's neurons are dynamical in the concept that their output is communicated back to their input via delayed units. The diagonal weight (W_D) ensures the feedback. As a result, the local circuits are responsible for the network's dynamic behavior. Besides, by zeroing vector W_D , HLRNN is reduced to Multi-Layer Feed-Forward Neural Network (MLFFNN). The output layer contains two neurons that represent the PI Controller's gains. The connection between hidden and output layer neurons is represented by the output weight vector (W_o).

The power plant system is controlled by six PI regulators based on the HLRNN algorithm. The structure of each Controller is chosen based on the trial-and-error method until the desired performance is achieved. So, the MPPT algorithm is calculated using the first controller. The second and third are employed to perform rotor current. The fourth is set up to maintain the DC-Link voltage constant. The fifth and sixth are in charge of the grid currents. Based on the structure illustrated in Fig 2, the controllers of the system can be designed as shown in the following subsections.

4.2.2. HLRNN-based MPPT controller

Fig. 3 depicts the control process design for MPPT controller, by adopting the hidden layer recurrent neural network methodology to tune the PI regulator's gains. The HLRNN-MPPT controller is designed with three neurons in the input layer, seven neurons in the hidden layer, and two neurons in the output layer (3-7-2 structure).

4.2.3. Implementing the RSC controller based on the HLRNN method

Fig. 4 illustrates the control process design for Rotor side converter, which is based on the HLRNN methodology used to self-adapt the PI regulator's settings. The HLRNN-RSC 1 and 2 Controllers are designed using a 3-10-2 structure.

4.2.4. Designing the GSC and DC link controllers optimized by the HLRNN method

Fig. 5 shows the GSC and DC-link voltage control process based on the hidden layer recurrent neural network approach, which is dedicated to optimize the PI regulator's gains. The GSC Controller is designed using the 3-10-2 architecture. The HLRNN DC-Link Controller, on the other hand, is based on a 3-8-2 structure.

The PI regulators, illustrated in Figs. 3-5, are tuned by minimizing the cost function mean square error (MSE), which is defined by the following equation:

$$E_j(k) = \frac{1}{2} (y_j(k) - y_{nnj}(k))^2 \quad (46)$$

Where $y(k)$ defines the output responses of the system, which are wind turbine's rotational speed (Ω_{rot_mec}), rotor current components (i_{rot_d} and i_{rot_q}), grid currents (i_{gsc_d} and i_{gsc_q}), and DC-Link voltage (V_{DC}). However, $y_{nn}(k)$ denotes the output responses of the HLRNN structure, which are: V_{denn} , i_{gsc_dnn} , i_{gsc_dnn} , i_{rot_dnn} , i_{rot_qnn} , and Ω_{rot_mecnn} .

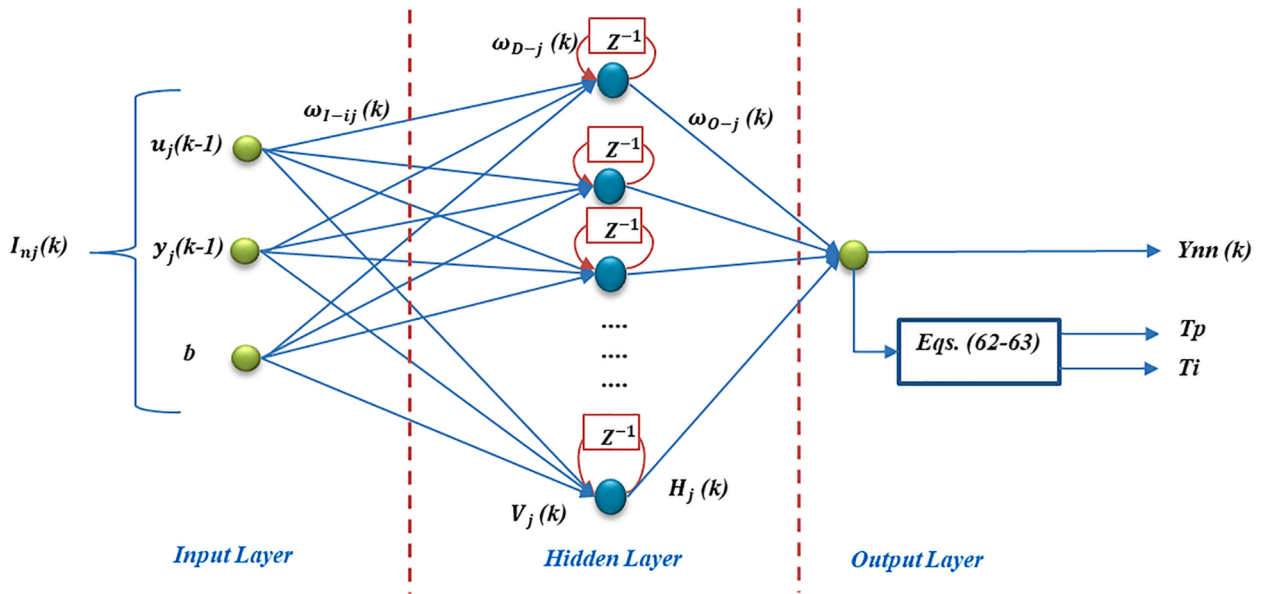


Fig 2. Structure of HLRNN.

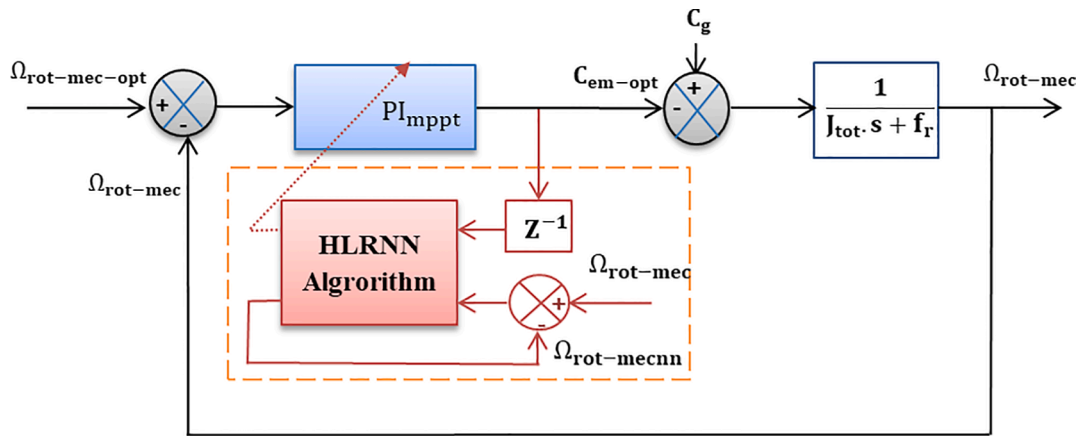


Fig 3. MPPT Controller based on HLRNN method.

4.3. Mathematical equations of the HLRNN algorithm

The initial layer of the HLRNN structure is composed of three components which constitute the vector input below:

$$I_{nj}(k) = [u_i(k-1)y_i(k)b], \text{ With } b = 1 \text{ and } k \text{ is the discrete - time signal} \quad (47)$$

Where $y_j(k)$ is the actual output of j^{th} neuron, b denotes the bias, and $u_j(k-1)$ represents the delayed control command input of the HLRNN algorithm. Therefore, the actual control algorithm is defined by transforming Eq. (45) into a recurrence equation as follows:

$$u_j(k) = T_{pj}(k) \cdot x_{c1j} + T_{ij}(k) \cdot x_{c2j} \quad (48)$$

Where

$$x_{c1j} = e_j(k); x_{c2j} = \sum e_j(k) \quad (49)$$

$e_j(k)$ is the error between desired output and the observed output of the system. T_p and T_i are the Controller's Proportional and Integral gains, respectively.

The vector input of the recurrent j^{th} neuron is described by the following sum vector ($V_j(k)$):

$$V_j(k) = (I_{nj}(k)) \cdot \omega_{ij} + \omega_{Dj} \cdot H_j(k-1) \quad (50)$$

Where $w_{Dj}(k)$ is the weight vector of the recurrent hidden layer $H_j(k)$ is the output of the hidden layer and is activated using the hyperbolic tangent function as below:

$$H_j(k) = f(V_j(k)) = \frac{1 - e^{-V_j}}{1 + e^{-V_j}} \quad (51)$$

The output vector of the HLRNN ($Y_{nnj}(k)$), as shown in Fig 2, is expressed as follows:

$$y_{nnj}(k) = \sum_{i=1}^{N_d} y_{nnj}(k-1) + \omega_{Oj}(k) \cdot H_j(k) \quad (52)$$

Where $w_{Oj}(k)$ is the weight vector of the output layer. The hidden layer recurrent neural network's learning is ensured by updating the weights of each neuron to optimize the fitness function specified in Eq. (45). Furthermore, the gradient descent learning approach with momentum term is utilized to update the input, recurrent, and output layers in the following manner [20,51]. Besides, the addition of momentum as a fixed factor decreases the fluctuation tendency of the learning activity and enhances convergence [52].

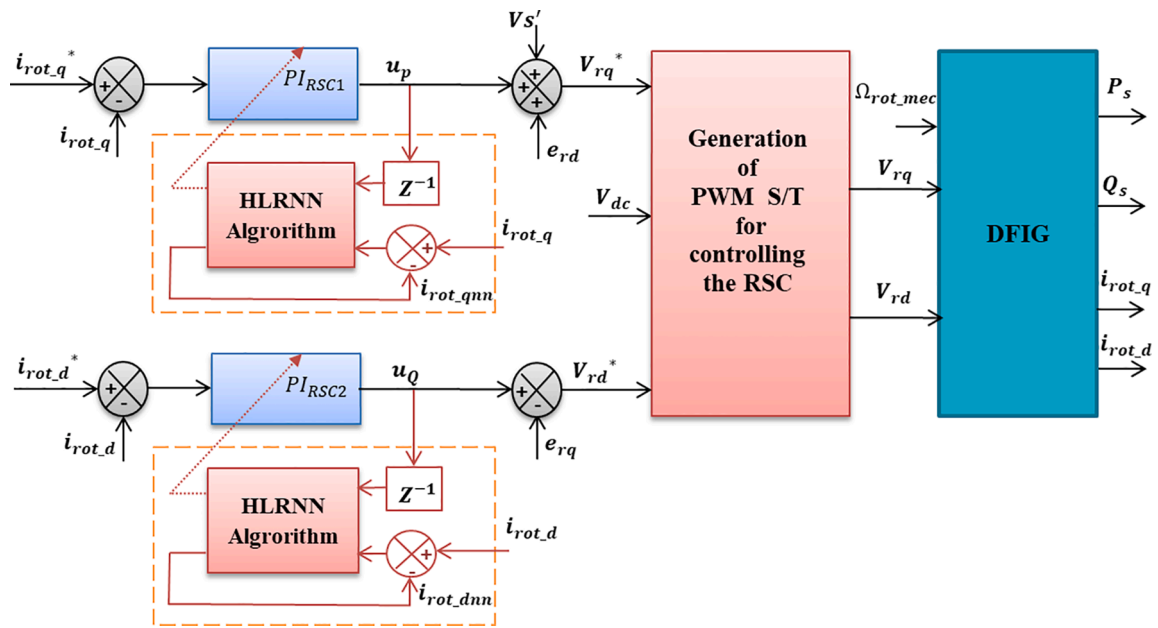


Fig 4. PI Controller Design for RSC based on HLRNN architecture.

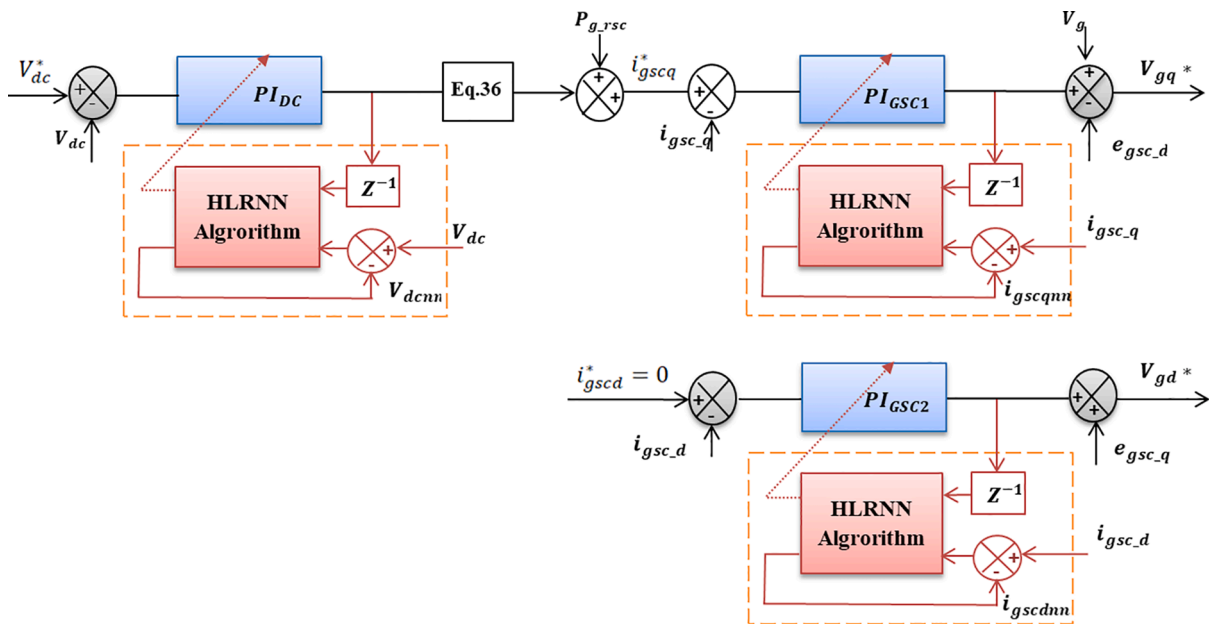


Fig 5. PI Controller based on HLRNN architecture for GSC and DC-Link voltage.

$$\omega_{ij}(k) = \omega_{ij}(k-1) + \rho_{ij} \cdot \left(-\frac{\partial E}{\partial \omega_{ij}^1} \right) + \mu_j \cdot ((\omega_{ij}(k-1) - \omega_{ij}(k-2))) \quad (53)$$

$$\omega_{Dj}(k) = \omega_{Dj}(k-1) + \rho_{Dj} \cdot \left(-\frac{\partial E}{\partial \omega_{ij}^D} \right) + \mu_j \cdot ((\omega_{Dj}(k-1) - \omega_{Dj}(k-2))) \quad (54)$$

$$\omega_{Oj}(k) = \omega_{Oj}(k-1) + \rho_{Oj} \cdot \left(-\frac{\partial E}{\partial \omega_{ij}^O} \right) + \mu_j \cdot ((\omega_{Oj}(k-1) - \omega_{Oj}(k-2))) \quad (55)$$

$$-\frac{\partial E}{\partial \omega_{ij}^1} = e(k) \cdot \frac{\partial Y_{nn}(k)}{\partial H_j(k)} \cdot \frac{\partial H_j(k)}{\partial \omega_{ij}^1} = e(k) \cdot \omega_j^O \cdot Z_{ij}(k) \quad (56)$$

$$-\frac{\partial E}{\partial \omega_{ij}^D} = e(k) \cdot \frac{\partial Y_{nn}(k)}{\partial H_j(k)} \cdot \frac{\partial H_j(k)}{\partial \omega_{ij}^D} = e(k) \cdot \omega_j^O \cdot T_j(k) \quad (57)$$

$$-\frac{\partial E}{\partial \omega_{ij}^O} = e(k) \cdot \frac{\partial Y_{nn}(k)}{\partial \omega_{ij}^O} = e(k) \cdot H_j(k) \quad (58)$$

Where

$$T_j = \frac{\partial H_j(k)}{\partial \omega_{ij}^D} = \sum_{j=1}^{Nd} \omega_{Oj}(i) \cdot (1 + H_j(i)) \cdot (1 - H_j(i)) \cdot \varphi_j(i); \text{ With } T_j(0) = 0 \quad (59)$$

Let us compute the partial derivative of the cost function with respect to the weights:

$$Z_{ji} = \frac{\partial H_j(k)}{\partial \omega_{ij}^l} = \sum_{i=1}^{N_d} \sum_{j=1}^{N_{in}} \omega_{Oj}(i) \cdot (1 + H_j(i)) \cdot (1 - H_j(i)) \cdot \text{In}_j(k); \text{ With } Z_{ji}(0) = 0 \quad (60)$$

Where N_{in} and N_d are the number of the neurons in first and dynamic cell, respectively. ρ_{Ij} , ρ_{Dj} , and ρ_{Oj} are the learning rate of the input, hidden, and output cell, respectively, μ_j is the momentum constant. A learning rate should be specified for each training algorithm. The learning rates are chosen based on the testing method. In this work, learning rates were tested with smaller values until a satisfactory result was obtained. However, the maximum learning is occurred in the range [-0.5, 0.5] [53].

If

$$|w_{Dj}(k)| > 1$$

then

$$w_{Dj}(k) = \frac{1}{2} \cdot \text{sign}(w_{Dj}(k)) \quad (61)$$

Finally, the gains of the PI controller can be tuned and updated according to gradient descent as follows:

$$T_{Pj}(k) = T_{Pj}(k-1) + Y_{nn}(k) \cdot e_j(k) \cdot x_{c1j} \quad (62)$$

$$T_{Ij}(k) = T_{Ij}(k-1) + Y_{nn}(k) \cdot e_j(k) \cdot x_{c2j} \quad (63)$$

4.4. Proposed algorithm flowchart

The steps for generating the programming code in Matlab script are organized as shown in the flowchart in Fig 6. The MPPT Controller sub-program is used as an example, and the other sub-programs will be examined in the same way.

5. Simulation and results

5.1. Simulation data

The wind energy plant system based on the dual-fed induction generator is modeled using previously established equations and simulated employing Matlab/Simulink. Based on the flowchart (Fig 6), a main program code of the hidden layer recurrent neural network control has been constructed in the employed software's script, in which six sub-programs are invoked, each of which is destined for tuning one PI controller parameters. Fixed values are assigned to the learning rate and inertia coefficients of the input, hidden, and output layers. Table 1 shows the parameters utilized in the simulation for the system comprised of the 5 MW wind turbine, DFIG, capacitor, and the serial resistance inductance (RL) filter.

Two bidirectional converters, rotor side and grid side converter, are employed to pilot the generator. The proposed control is developed to create pulse width modulation (PWM) for optimal converters regulation. The PI gains have been automatically adjusted to achieve the best response for the studied system. According to the error function formulation, the mean square error is reduced when the PI regulator parameters are tuned to the optimal gains illustrated in the Table 2.

5.2. Results and discussion

The effectiveness and robustness of the hidden layer recurrent neural network (HLRNN) method are demonstrated under normal conditions, generator parameter variations, and grid phase short-circuited faults.

5.2.1. Normal conditions

This section displays the simulation results of the rotor wound in-

duction generator, which is powered by a wind turbine and connected to the electricity grid. To determine the grid voltage components, the Park transformation is employed, which is based on the angle transformation estimated by the Phase-Locked Loop (PLL) with the PI Controller. Fig. 8 depicts the grid's quadrature and direct voltages utilized to supply the generator. Moreover, Fig 9 shows the wind turbine coefficient of power derived using the two techniques. As it might be seen, the HLRNN keeps the C_p parameter at its optimal point ($C_{pmax} = 0.5$), the TSR at its optimum ($\lambda_{-Tu-opt} = 9.19$), and the aerodynamic power at its maximum. Furthermore, the change in wind speed is disallowed in court time. Fig. 10 depicts the mechanical rotational velocity attained using the MPPT methodology based on the PI controller and HLRNN strategy. In comparison to the other technique, the HLRNN method provides a shorter time, estimated at 0.02 (m s), for following the speed reference without overshoot. The MPPT algorithm is utilized to create the reference stator active power (P_s^*). Fig. 11 depicts the stator active power calculated by the investigated controllers. By comparing these results, it is noticeable that the produced power rapidly follows the reference (P_s^*) when the hidden layer neural network is used rather than the indirect vector control (IFOC), with superior performance in terms of rapidity and precision. Fig. 12 illustrates the reactive power, which is set to zero to maintain a unit power factor. Fig. 13 describes the effect of wind speed change on DC-Link voltage. As we can see, every change in wind speed causes a voltage overshoot. Besides, the proposed technique has less voltage overshoot than the IFOC.

We can affirm that the main benefit of the hidden layer recurrent neural network is that it swiftly eliminates wind disturbances while maintaining the DC-link voltage constant with a zero error. Similarly, the suggested technique improves overshoot significantly more than classical PI controllers. Table 3 shows the comparison results for the two methods. The nominal active power is 5 MW, the rotational speed is rated at 105.2 rad/s, and the DC link voltage is rated at 1200 V. As can be shown, the HLRNN outperforms the indirect vector control based on the PI Controller. The proposed technique minimizes overshoot, significantly reduces response time, and attenuates static error.

5.2.2. Variation in DFIG settings

This part puts the hidden layer recurrent neural network to the test against unanticipated changes in the generator's intrinsic settings. Many situations are taken into consideration for this objective. First, the rotor's resistance is modified by 100% (the case where the rotor resistance is warming up). When the HLRNN technique is employed, the response time is the same, but it is increased to 11.7 (m s) with an error of 1.78% when the indirect vector control based on the conventional PI controller is utilized, as shown in Fig 14. In the second case, the rotor inductance value is altered by a factor of 100%. Fig. 15 indicates that the output power is guaranteed to be stable with a minimal increase in response time of the order of 4.6 (m s). When the IFOC approach is used, response time becomes 29.2 (m s). Furthermore, the system's stability is affected. The third scenario involves increasing the rotor resistance and inductance by 100% of their rated values, as illustrated in Fig 16. In this instance, HLRNN outperforms IFOC in terms of precision and stability. Finally, the fourth situation examines the effect of increasing the stator inductance to 100% on the generated power, as shown in Fig 17. When the HLRNN approach is used, a power overshoot of the order of 1.74% is observed, which is regarded as negligible. The response time grew from 1.8 (m s) to 5.2 (m s), maintaining the system's stability. When the indirect vector control is utilized, the response time is raised to 13 (m s), and the system's stability is lost.

These findings lead us to conclude that hidden layer recurrent neural network control is more robust and efficient in terms of system stability and response time.

5.2.3. Grid fault conditions

The fault analysis is conducted for variable wind speeds and when the speed is at its rated value for asymmetrical grid faults such as Line-

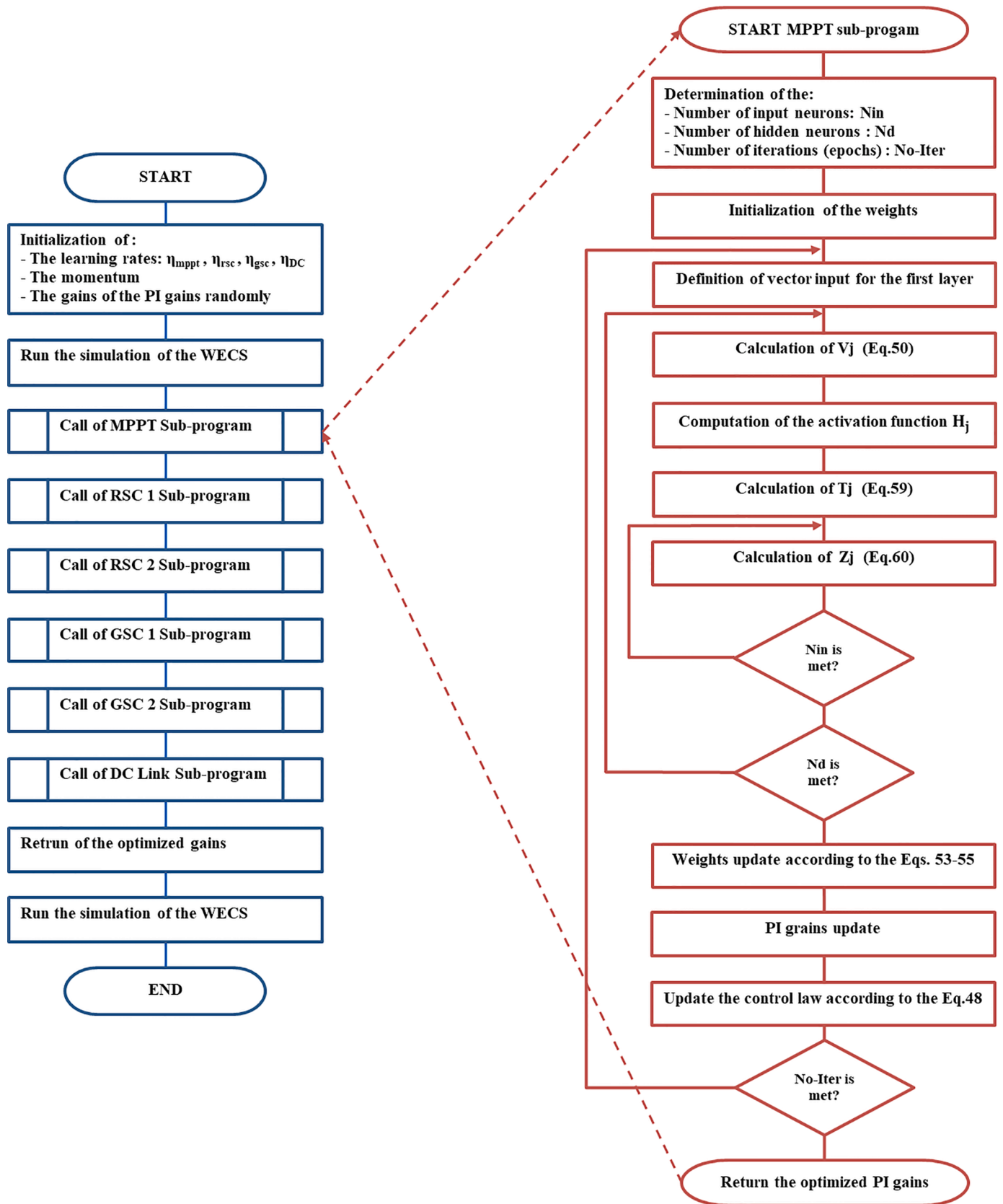


Fig 6. Flowchart of the HLRNN Algorithm.

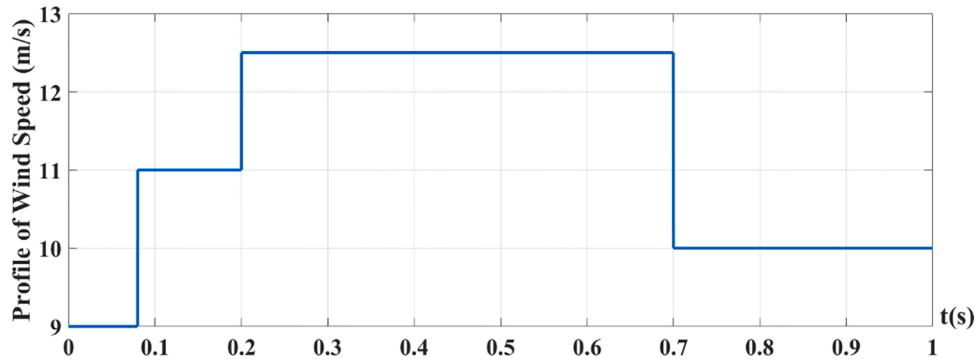


Fig 7. Wind energy speed profile (m/s).

Table 1
Parameters of wind power plant system components.

| | Parameters | Symbol | Values |
|-----------|-----------------------------|-----------|------------------------|
| Turbine | Radius of blade | R | 51.583 m |
| | Coefficient of multiplier | G_{Box} | 47.23 |
| | Total moment of inertia | J_{tot} | 1000 kg.m ² |
| DFIG | DFIG rated power | P_s | 5 MW |
| | Stator leakage inductance | L_{sta} | 1.2721 mH |
| | Rotor resistance | R_{rot} | 1.446 mΩ |
| | Rotor leakage inductance | L_{rot} | 1.1194 mH |
| | Mutual inductance | L_m | 0.55187 mH |
| | Stator line to line voltage | V_{gr} | 950 V |
| Capacity | DC-link capacitance | C | 4400 μF |
| Filter RL | Resistor of the filter | R_f | 20 Ω |
| | Inductance of the filter | L_f | 0.08 H |

to-Ground, Line-to-Line-to-Ground, and Line-to-Line. The fault block contained in Matlab/Simulink is used to perform the fault diagnosis. Therefore, the predefined default values of grid fault parameters are considered, which are illustrated in Table 4. Besides, the grid fault appeared at 0.4 (s) and was cleared at 0.6 (s) while remaining 200 (m s).

Figs. 18 and 19 show the reaction of the stator active power and the DC-Link voltage, respectively, in the case of the line-to-ground (L2G) fault, employing the two examined strategies. As shown in Fig 18, the highest oscillations around the nominal value are reduced from 32.02%, for indirect vector control based on a traditional PI controller, to 29.82%, for hidden layer recurrent neural network control (HLRNN).

Table 2
Optimal gains of different controllers.

| | MPPT Controller | | RSC1 Controller | | RSC2 Controller | | GSC1 Controller | | GSC2 Controller | | DC-Link Controller | |
|--------|-----------------|---------|-----------------|-------|-----------------|-------|-----------------|---------|-----------------|---------|--------------------|----------|
| Gains | T_p | T_i | T_p | T_i | T_p | T_i | T_p | T_i | T_p | T_i | T_p | T_i |
| Values | -5.56e+7 | 1.84e+2 | 1.427 | 1.237 | 0.686 | 1.872 | 6.24e+3 | 1.47e+2 | 3.232e+4 | 1.66e+2 | 1.991 | 4.499e+2 |

The wind energy velocity used to model the system is depicted in Fig. 7.

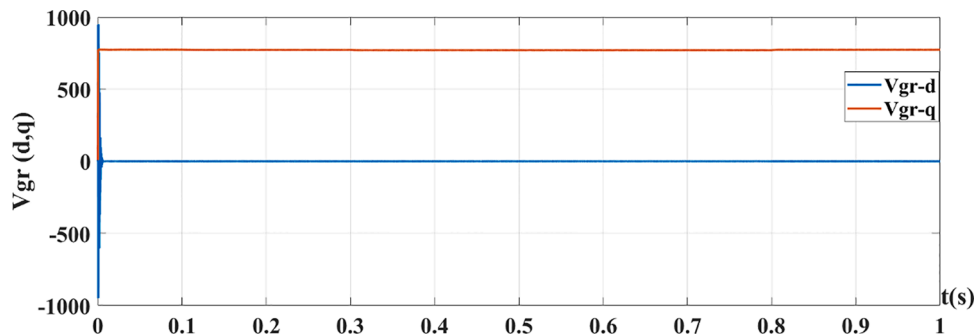


Fig 8. dq components of grid voltage (V).

After the fault is cleared, the active power curve remains at its reference with a reduced response time of 14.4 (m s) when using HLRNN compared to 23.3 (m s) when using the traditional PI Controller. Fig. 19 depicts voltage oscillations of the DC link capacitor during a line-to-ground fault. When HLRNN is used, the peak value is reduced from 23.92% to 13.42%. Figs. 20 and 21 depict the response of the active power and the DC-link voltage to the double-line-to-ground (LL2G) failure using the two investigated techniques. HLRNN reduces oscillations for this fault type from 75.04% to 35.26%, as shown in Fig 20. After the problem is resolved, the response time is lowered from 35.6 (m s) to 16.6 (m s) when the proposed control is utilized. However, when HLRNN is applied, a static error of 8.82% is observed, while a static error of 2.92% is recorded when indirect vector control based on PI Controller is employed. Fig. 21 displays voltage oscillations of the DC link capacitor during the LL2G fault. The maximum value of ripples is reduced from 23% to 12%. Besides, the response time is improved from 38.5 (m s) to 19.2 (m s) when HLRNN is employed. Figs. 22 and 23 illustrate the influence of line-to-line (L2L) short circuit using the two strategies tested on active power and DC-link voltage, respectively. As seen in Fig 22, HLRNN lowers oscillations for this fault type from 83.93% to 53.6%. After the problem is overcome, the proposed control reduces the response time from 26.7 (m s) to 19.9 (m s). During the LL2G fault, the voltage oscillations of the DC-Link capacitor are shown in Fig 23. When HLRNN is used, the maximum value of ripples is lowered from 37.83% to 16.41% and the response time is reduced to 16.4 (m s) from 19 (m s).

These results show that hidden layer recurrent neural network control of a wound rotor induction generator provides robustness against

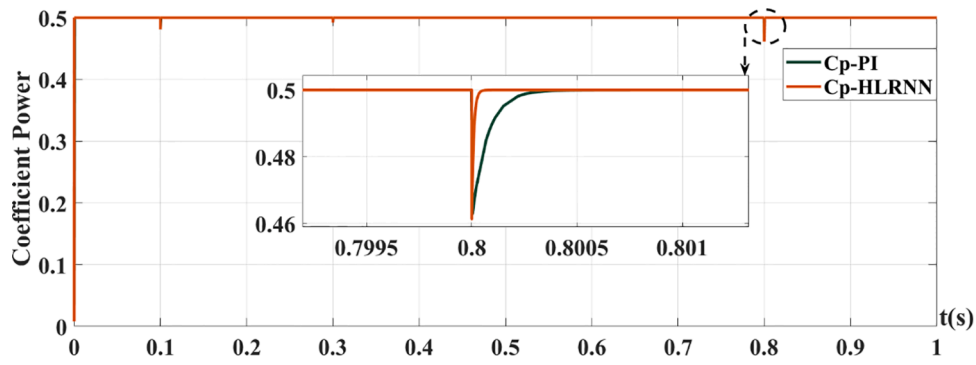


Fig 9. Wind turbine power factor.

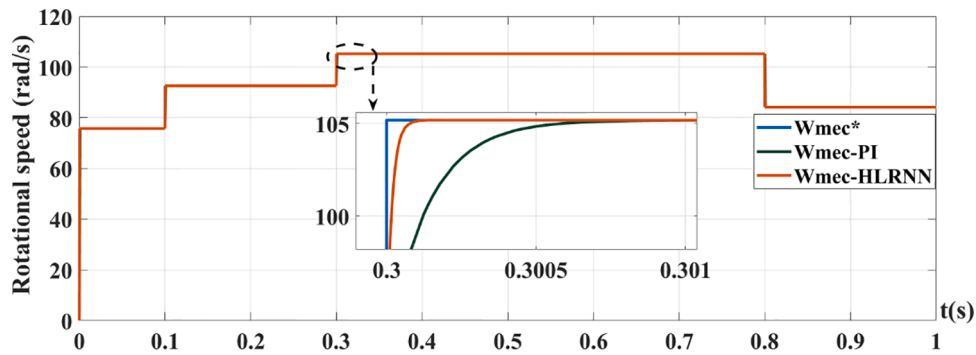


Fig 10. Mechanical rotational speed (rad/s).

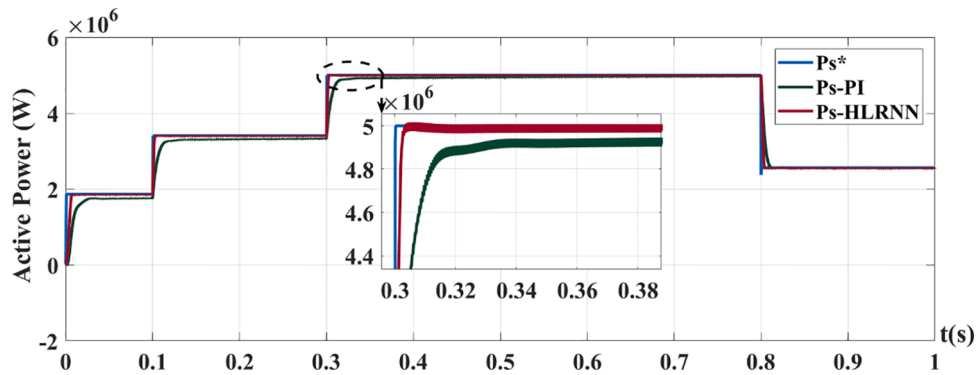


Fig 11. Stator active power (W).

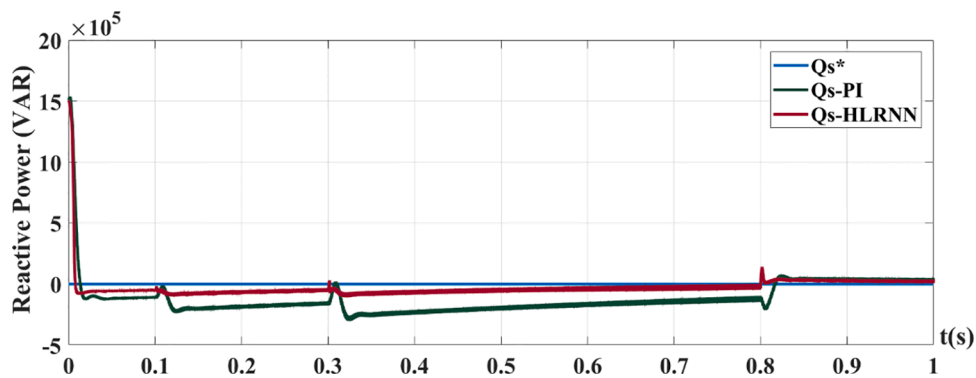


Fig 12. Reactive power (VAR).

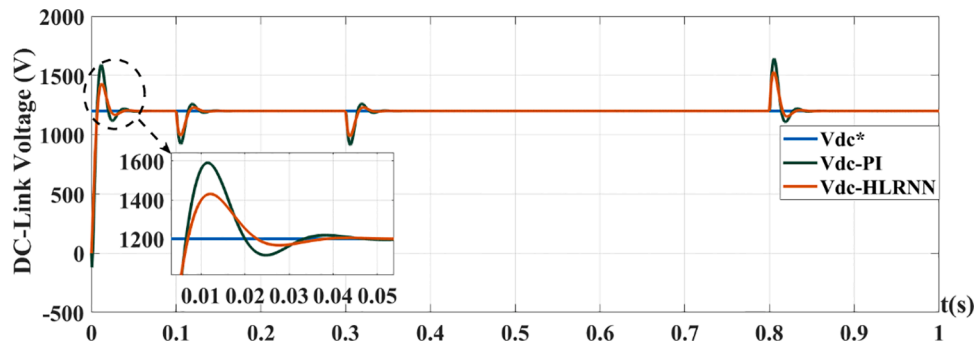


Fig 13. DC-Link voltage (V).

Table 3
Summary of the two approaches outcomes.

| Performances | Active power | | Rotational speed | | DC-link voltage | |
|---------------------|--------------|-------|------------------|-------|-----------------|-------|
| | PI | HLRNN | PI | HLRNN | PI | HLRNN |
| Response time (m s) | 10.1 | 1.8 | 0.1 | 0.02 | 28 | 26 |
| Static error% | 1.42 | 0.16 | 0 | 0 | 0 | 0 |
| Overshoot% | - | 0.24 | - | - | 32.41 | 19.08 |

grid asymmetrical faults while providing electricity production with reduced overshoot and a fast response time when the failure is corrected.

5.2.4. Comparison study to other existing neural network schemes

Table 5 compares the proposed methodology to current neural network control approaches reported in the literature. Response time, steady-state error, and overshoot are utilized as criteria in this comparison. With a shorter response time and a reduced overshoot, the

hidden layer recurrent neural network strategy outperforms the other methods.

6. Conclusions

The entire wind chain is modeled using the before-mentioned equations and controlled by two proposed methods: the Indirect Field-Oriented Control and the Hidden Layer Recurrent Neural Network. The system is simulated employing Matlab/Simulink software and the script to establish the program code. A changeable wind velocity profile is chosen and used to train the system. The DFIG stator is directly connected to the power grid, while the rotor is linked via two pulse width modulation AC/DC/AC converters to the electric grid. Maximum Power Point Tracking is established in a closed-loop with speed control. Then, the stator powers are managed using indirect field-aligned vector control and intelligent neural network control to enhance the dynamical performance of the system. Finally, the generator’s robustness and effectiveness are tested by altering all its settings and are examined

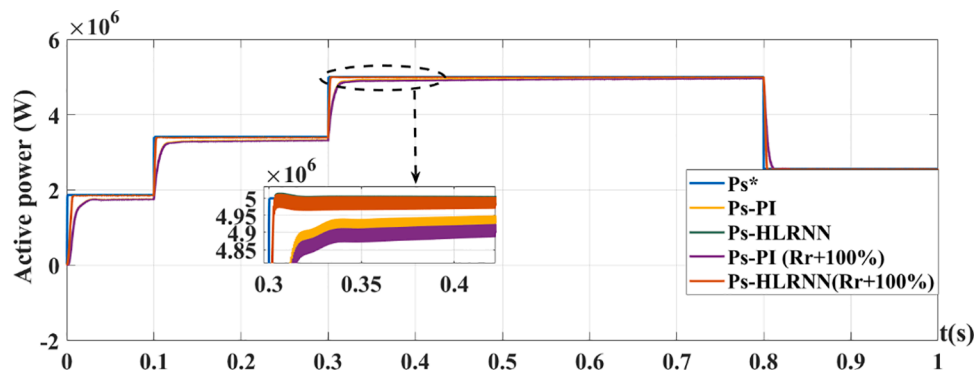


Fig 14. Active power ($R'_{rot} = 2 \cdot R_{rot}$).

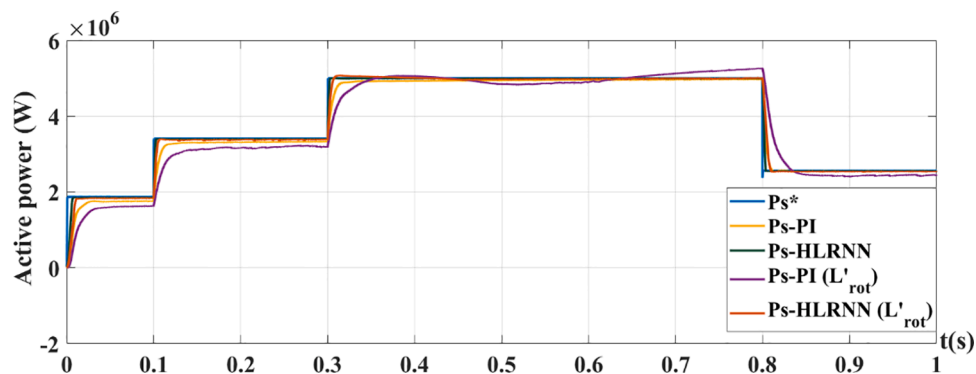


Fig 15. Active power ($L'_{rot} = 2 \cdot L_{rot}$).

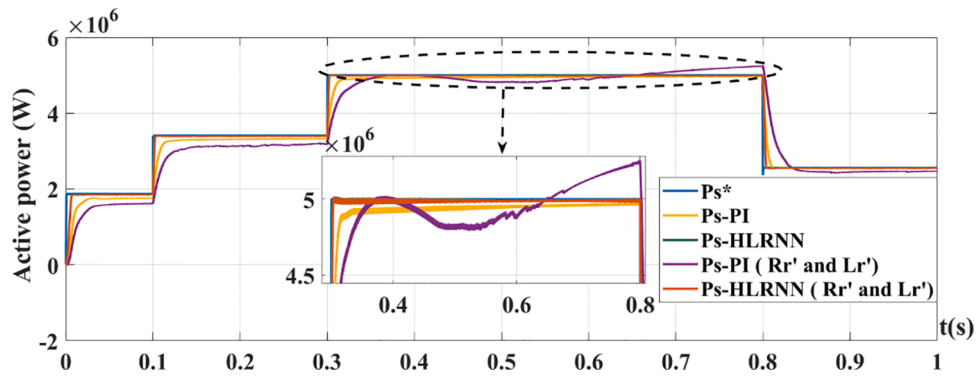


Fig 16. Active power ($R'_{rot} = 2 \cdot R_{rot}$ and $L'_{rot} = 2 \cdot L_{rot}$).

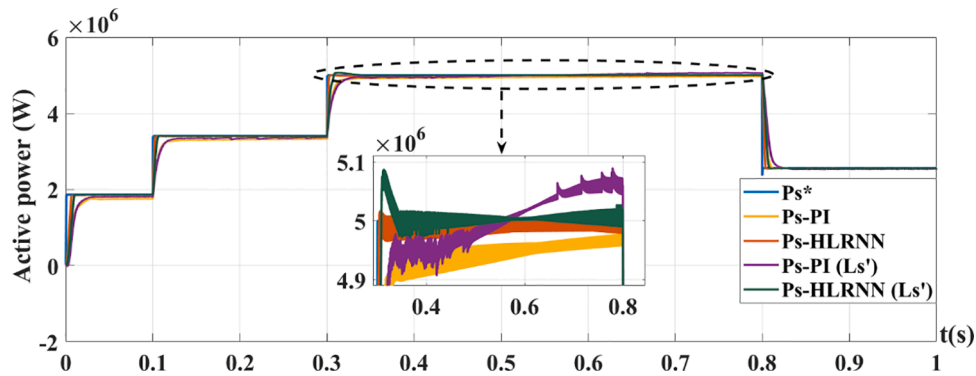


Fig 17. Active power ($L'_{sta} = 2 \cdot L_{sta}$).

Table 4
Grid fault parameters.

| Parameter | Fault resistance R_{on} | Ground resistance R_g | Snubber resistance R_s |
|-------------|------------------------------|----------------------------|-----------------------------|
| Value (ohm) | 0.001 | 0.001 | 1e+6 |

under power grid voltage dips caused by different asymmetrical grid faults. According to the simulation results:

- The response time of the hidden layer recurrent neural network (HLRNN) is ameliorated to 1.8 (m s) compared to some recent neural network architectures and the indirect vector control. Furthermore, the HLRNN guarantees a reference track with an improved static error of 0.16%.

- The HLRNN outperforms the IFOC in terms of DC-link voltage control during wind speed changes. The response time is lowered to 0.026 s from 0.028 s when the Indirect Vector Control is applied. Additionally, the overshoot is minimized to 19.08% from 34.41%.
- The HLRNN method reveals better results than the indirect vector control in terms of robustness to variations in generator parameters and asymmetrical grid faults. When subjected to the investigated conditions, the HLRNN improves stability, increases precision, and decreases system reaction time.

Funding

This research received no external funding.

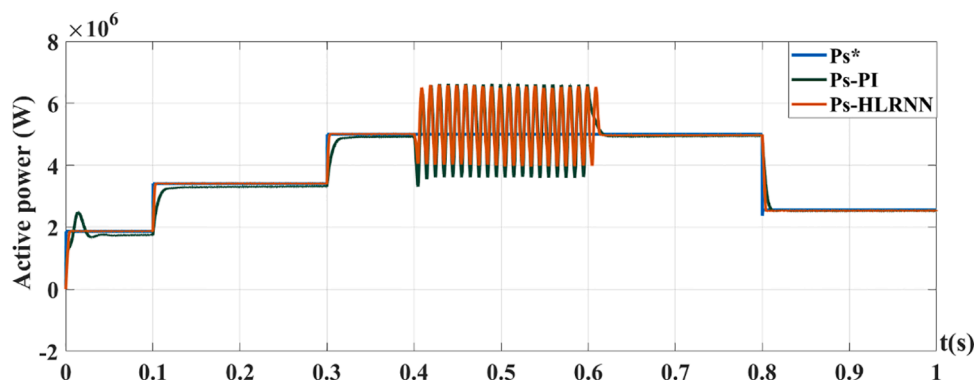


Fig 18. Active power in the case of a line-to-ground fault (L2G).

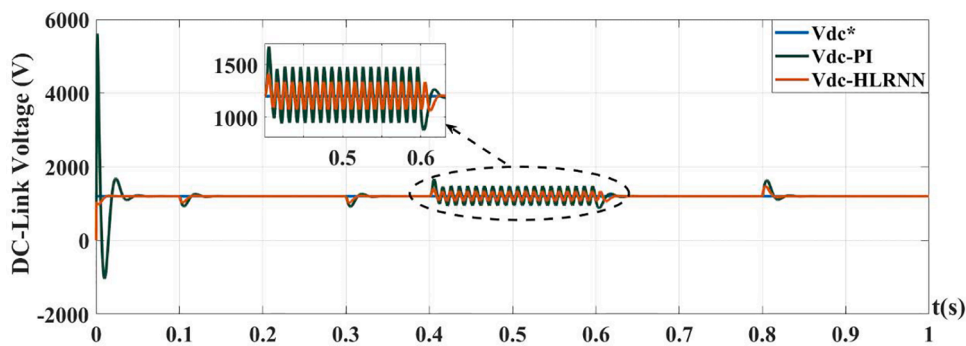


Fig 19. DC-link voltage in the state of a line-to-ground fault (L2G).

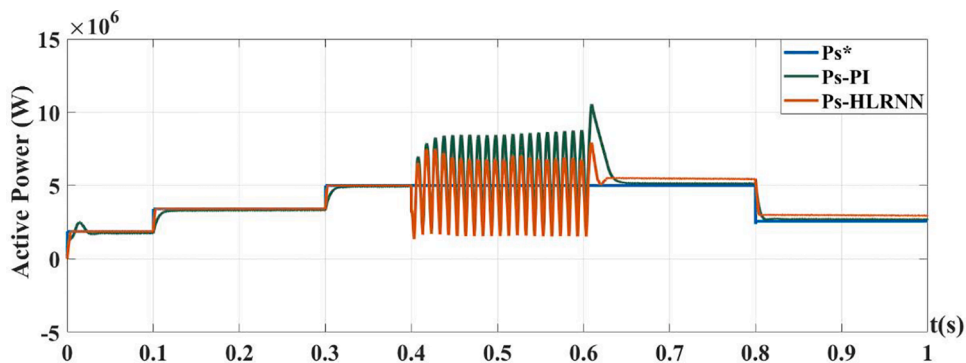


Fig 20. Active power in the state of a two-line to ground fault (LL2G).

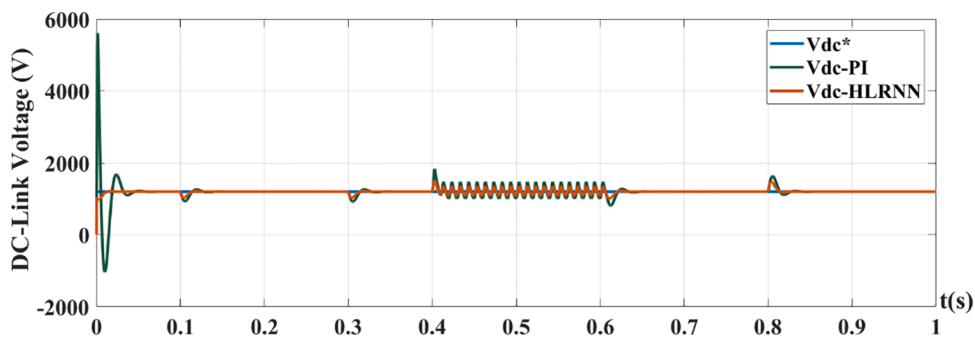


Fig 21. DC-link voltage in the situation of a two-line to ground fault (LL2G).

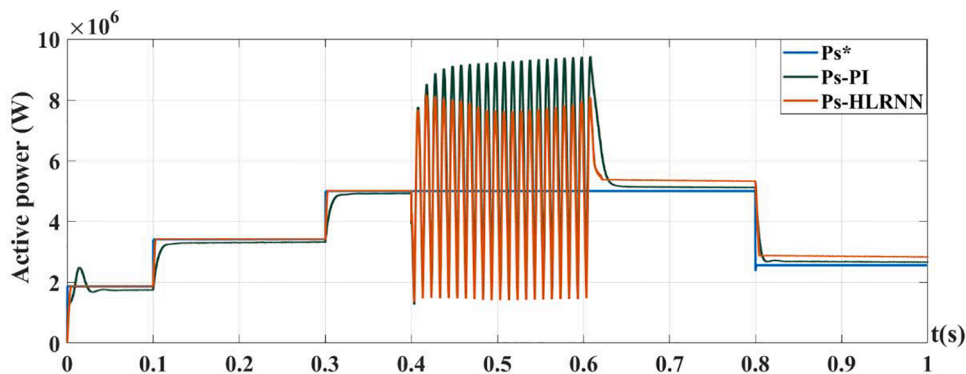


Fig 22. Active power in the case of a line-to-line fault (L2L).

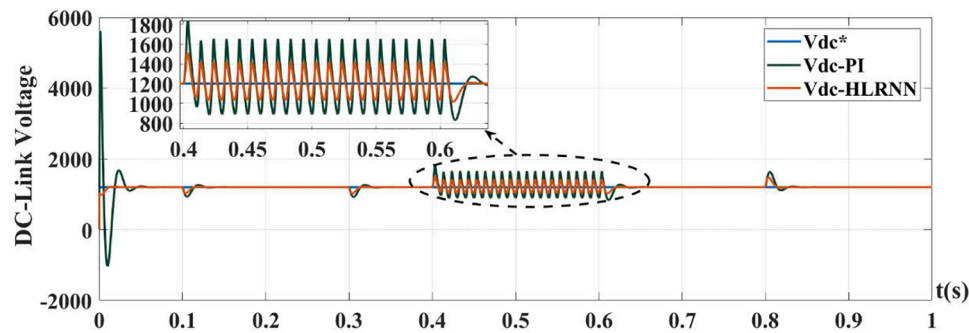


Fig 23. DC-link voltage in the case of a line-to-line fault (L2L).

Table 5

Analysis of the proposed method in comparison to other existing neural network schemes for the same generator.

| Paper reference | Method | Response time (s) | Static error% | Overshoot % |
|-----------------------------------|--------|-------------------|---------------|-------------|
| H. Benbouhenni et al. (2021) [12] | NDVC | 1, 78 | – | – |
| Rajasingam et al. (2019) [40] | DLNN | 0.1933 | – | 0 |
| D. Khan et al. (2020) [41] | RBFNN | 1.33 | – | 38 |
| J. Tavoozi et al. (2022) [42] | RT2FNN | 1.7 | – | 0.32 |
| B. Boudjellal et al. (2020) [43] | ANN | 0.028 | – | – |
| Proposed Control | HLRNN | 0.0018 | 0.16 | 0.24 |

Future work

In this work, we observe that the proposed control reduces the peak value of active power and the voltage in the capacitor caused by short-circuit voltage sags. As a result, Flexible AC Transmission Systems (FACTS) may be requested in the event of a grid fault and can be proposed as future work for this study.

CRedit authorship contribution statement

Elmostafa Chetouani: Conceptualization, Methodology, Software, Writing – original draft. **Youssef Errami:** Supervision, Validation, Writing – review & editing. **Abdellatif Obbadi:** Supervision, Validation, Writing – review & editing. **Smail Sahnoun:** Supervision, Validation, Writing – review & editing.

Declaration of Competing Interest

The authors declare no conflict of interest.

Data availability

Data will be made available on request.

References

- [1] A. Kadri, H. Marzougui, F. Bacha, Implementation of direct power control based on stator flux estimation using low-pass filter estimator for doubly fed induction generator–wind energy conversion system, *Proc. Inst. Mech. Eng. Part I J. Syst. Control Eng.* 233 (7) (2019) 764–778, <https://doi.org/10.1177/0959651818818895>.
- [2] B. Azeem, et al., Robust neural network scheme for generator side converter of doubly fed induction generator, 2017 Int. Symp. Recent Adv. Electr. Eng. RAEE (2017) 1–6, <https://doi.org/10.1109/RAEE.2017.8246149>, vol. 2018-Janua2017.
- [3] E. Chetouani, Y. Errami, A. Obbadi, S. Sahnoun, B. Wadawa, Nonlinear Backstepping with integral action for wind power plant based on doubly fed induction generator connected to the non-ideal grid, *Technol. Econ. Smart Grids Sustain. Energy* 7 (1) (2022), <https://doi.org/10.1007/s40866-022-00130-5>.
- [4] A.G. Abo-Khalil, W. Alharbi, A.R. Al-Qawasmi, M. Alobaid, I. Alarifi, Modeling and control of unbalanced and distorted grid voltage of grid-connected DFIG wind turbine, *Int. Trans. Electr. Energy Syst.* 31 (5) (2021) 1–21, <https://doi.org/10.1002/2050-7038.12857>.
- [5] A. Sobhy, A.G. Abo-Khalil, D. Lei, T. Salameh, A. Merabet, M. Alkasrawi, Coupling DFIG-based wind turbines with the grid under voltage imbalance conditions, *Sustain* 14 (9) (2022), <https://doi.org/10.3390/su14095076>.
- [6] G.S. Kaloi, J. Wang, M.H. Baloch, Active and reactive power control of the doubly fed induction generator based on wind energy conversion system, *Energy Rep.* 2 (2016) 194–200, <https://doi.org/10.1016/j.egy.2016.08.001>.
- [7] E. Bekiroglu and M.D. Yazar, “MPPT control of Grid connected DFIG at variable wind speed,” *Energies*, vol. 15, no. 9, 2022, doi: 10.3390/en15093146.
- [8] B. Pavan Babu, V. Indragandhi, Analysis of back to Back (BTB) converter control strategies in different power system applications, *IOP Conf. Ser. Mater. Sci. Eng.* 906 (1) (2020), <https://doi.org/10.1088/1757-899X/906/1/012016>.
- [9] E. Chetouani, Y. Errami, A. Obbadi, S. Sahnoun, Design of optimal backstepping control for a wind power plant system using the adaptive weighted particle swarm optimization, *Int. J. Intell. Eng. Syst.* 14 (6) (2021) 125–136, <https://doi.org/10.22266/ijies2021.1231.12>.
- [10] M. Bouderbala, B. Bossoufi, A. Lagrioui, M. Taoussi, H.A. Aroussi, Y. Ihedrane, Direct and indirect vector control of a doubly fed induction generator based in a wind energy conversion system, *Int. J. Electr. Comput. Eng.* 9 (3) (2019) 1531–1540, <https://doi.org/10.11591/ijece.v9i3.pp1531-1540>.
- [11] A.S.S. Vardhan, R. Saxena, Vector control of DFIG-based wind turbine system, *GMSARN Int. J.* 16 (4) (2022) 348–358.
- [12] H. Benbouhenni, N. Bizon, Advanced direct vector control method for optimizing the operation of a double-powered induction generator-based dual-rotorwind turbine system, *Mathematics* 9 (19) (2021), <https://doi.org/10.3390/math9192403>.
- [13] S. Boubzizi, H. Abid, A. El hajjaji, M. Chaabane, Comparative study of three types of controllers for DFIG in wind energy conversion system, *Prot. Control Mod. Power Syst.* 3 (1) (2018) 1–12, <https://doi.org/10.1186/s41601-018-0096-y>.
- [14] E. Chetouani, Y. Errami, A. Obbadi, S. Sahnoun, Optimal tuning of pi controllers using adaptive particle swarm optimization for doubly-fed induction generator connected to the grid during a voltage dip, *Bull. Electr. Eng. Inf.* 10 (5) (2021) 2367–2376, <https://doi.org/10.11591/eei.v10i5.2843>.
- [15] M.A. Soomro, Z.A. Memon, M. Kumar, M.H. Baloch, Wind energy integration: dynamic modeling and control of DFIG based on super twisting fractional order terminal sliding mode controller, *Energy Rep.* 7 (2021) 6031–6043, <https://doi.org/10.1016/j.egy.2021.09.022>.
- [16] H. Rahmaniard, T. Plaksina, Application of artificial intelligence techniques in the petroleum industry: a review, *Artif. Intell. Rev.* 52 (4) (2019) 2295–2318, <https://doi.org/10.1007/s10462-018-9612-8>.
- [17] A.A. Yesudhas, Y.H. Joo, S.R. Lee, Reference Model Adaptive Control Scheme on PMVG-Based WECS for MPPT under a Real Wind Speed, *Energies* 15 (9) (2022), <https://doi.org/10.3390/en15093091>.
- [18] I. Yaichi, A. Semmah, P. Wira, Control of doubly fed induction generator with maximum power point tracking for variable speed wind energy conversion systems, *Period. Polytech. Electr. Eng. Comput. Sci.* 64 (1) (2020) 87–96, <https://doi.org/10.3311/PPee.14166>.
- [19] C.J. Lin, C.C. Peng, C.H. Chen, H.Y. Lin, A self-organizing recurrent wavelet neural network for nonlinear dynamic system identification, *Appl. Math. Inf. Sci.* 9 (1) (2015) 125–132, <https://doi.org/10.12785/amis/091116>.
- [20] R. Kumar, S. Srivastava, J.R.P. Gupta, A. Mohindru, Diagonal recurrent neural network based identification of nonlinear dynamical systems with Lyapunov stability based adaptive learning rates, *Neurocomputing* 287 (2018) 102–117, <https://doi.org/10.1016/j.neucom.2018.01.073>.
- [21] A. Kazemy, S.A. Hosseini, M. Farokhi, Second order diagonal recurrent neural network, *IEEE Int. Symp. Ind. Electron.* (2007) 251–256, <https://doi.org/10.1109/ISIE.2007.4374607>. March.
- [22] R.A.D. Oliveira, M.H.J. Bollen, Magnification of transients at the voltage dips starting and its impacts on DFIG-based wind power plants, *Electr. Power Syst. Res.* 211 (2022), 108244, <https://doi.org/10.1016/j.epr.2022.108244>. June.

- [23] M.E. Meral, D. Çelik, Comparison of SRF/PI- and STRF/PR-based power controllers for grid-tied distributed generation systems, *Electr. Eng.* 100 (2) (2018) 633–643, <https://doi.org/10.1007/s00202-017-0530-6>.
- [24] M.Q. Duong, S. Leva, M. Mussetta, K.H. Le, A comparative study on controllers for improving transient stability of DFIG wind turbines during large disturbances, *Energies* 11 (3) (2018), <https://doi.org/10.3390/en11030480>.
- [25] M.Q. Duong, F. Grimaccia, S. Leva, M. Mussetta, K.H. Le, Hybrid controller for transient stability in wind generators, in: 2015 Clemson Univ. Power Syst. Conf. PSC 2015, 2015, <https://doi.org/10.1109/PSC.2015.7101690>.
- [26] D. Çelik, Lyapunov based harmonic compensation and charging with three phase shunt active power filter in electrical vehicle applications, *Int. J. Electr. Power Energy Syst.* 136 (April 2021) 2022, <https://doi.org/10.1016/j.ijepes.2021.107564>.
- [27] H. Ahmed, D. Çelik, Sliding mode based adaptive linear neuron proportional resonant control of Vienna rectifier for performance improvement of electric vehicle charging system, *J. Power Sources* 542 (2022), 231788, <https://doi.org/10.1016/j.jpowsour.2022.231788>, July.
- [28] Z. Li, H. Xu, Z. Wang, Q. Yan, Stability Assessment and Enhanced Control of DFIG-Based WTs during Weak AC Grid, *IEEE Access* 10 (2022) 41371–41380, <https://doi.org/10.1109/ACCESS.2022.3166810>.
- [29] M.J. Tahir, I.A. Latiff, M.U. Gul, M. Alam, M.S. Mazliham, Symmetrical and asymmetrical fault currents: evaluation to enhance the performance of 220KV grid station, *J. Telecommun. Electron. Comput. Eng.* 10 (1–3) (2018) 147–152.
- [30] G. Rashid, M.H. Ali, Asymmetrical fault ride through capacity augmentation of DFIG based wind farms by parallel resonance fault current limiter, *IEEE Power Energy Soc. Gen. Meet.* (2016), <https://doi.org/10.1109/PESGM.2016.7741506>, 2016-Novem.
- [31] J. Mohammadi, S. Afsharnia, S. Vaez-Zadeh, S. Farhangi, Improved fault ride through strategy for doubly fed induction generator based wind turbines under both symmetrical and asymmetrical grid faults, *IET Renew. Power Gener.* 10 (8) (2016) 1114–1122, <https://doi.org/10.1049/iet-rpg.2015.0586>.
- [32] H. Elaimani, A. Essadki, N. Elmouhi, R. Chakib, Comparative Study of the Grid Side Converter's Control during a Voltage Dip, *J. Energy* 2020 (2020) 1–11, <https://doi.org/10.1155/2020/7892680>.
- [33] E. Chetouani, Y. Errami, A. Obbadi, S. Sahnoun, Hybrid control using adaptive particle swarm optimization and integral backstepping control of grid-connected doubly fed induction generator, *Trends Sci.* 18 (23) (2021), <https://doi.org/10.48048/tis.2021.712>.
- [34] J. Pande, P. Nasikkar, K. Kotecha, V. Varadarajan, A review of maximum power point tracking algorithms for wind energy conversion systems, *J. Mar. Sci. Eng.* 9 (11) (2021) 1–30, <https://doi.org/10.3390/jmse9111187>.
- [35] H.H.H. Mousa, A.R. Youssef, E.E.M. Mohamed, State of the art perturb and observe MPPT algorithms based wind energy conversion systems: a technology review, *Int. J. Electr. Power Energy Syst.* 126 (2021), 106598, <https://doi.org/10.1016/j.ijepes.2020.106598>, PA.
- [36] R. Kumar, H.P. Agrawal, A. Shah, H.O. Bansal, Maximum power point tracking in wind energy conversion system using radial basis function based neural network control strategy, *Sustain. Energy Technol. Assess.* 36 (2019), 100533, <https://doi.org/10.1016/j.seta.2019.100533>, February.
- [37] A.A. Chhipa, et al., Adaptive neuro-fuzzy inference system-based maximum power tracking controller for variable speed wecs, *Energies* 14 (19) (2021), <https://doi.org/10.3390/en14196275>.
- [38] S. MAHFOUD, A. DEROUICH, N.E.L. OUANJLI, M. EL MAHFOUD, Enhancement of the direct torque control by using artificial neuron network for a doubly fed induction motor, *Intell. Syst. with Appl.* 13 (2022), 200060, <https://doi.org/10.1016/j.iswa.2022.200060>, January.
- [39] S. Labdai, N. Bounar, A. Boukkroune, B. Hemic, L. Nezli, Artificial neural network-based adaptive control for a DFIG-based WECS, *ISA Trans.* (2022), <https://doi.org/10.1016/j.isatra.2021.11.045> xxxx.
- [40] N. Rajasingam, D. Rasi, S.N. Deepa, Optimized deep learning neural network model for doubly fed induction generator in wind energy conversion systems, *Soft Comput* 23 (18) (2019) 8453–8470, <https://doi.org/10.1007/s00500-019-03947-y>.
- [41] D. Khan, J.A. Ansari, S.A. Khan, U. Abrar, Power optimization control scheme for doubly fed induction generator used in wind turbine generators, *Inventions* 5 (3) (2020) 1–13, <https://doi.org/10.3390/inventions5030040>.
- [42] J. Tavooosi, et al., A machine learning approach for active/reactive power control of grid-connected doubly-fed induction generators, *Ain Shams Eng. J.* 13 (2) (2022), 101564, <https://doi.org/10.1016/j.asej.2021.08.007>.
- [43] B. Boudjellal, T. Benslimane, *Modell Measurement Control A* 93 (1) (2020) 31–38.
- [44] Y. Errami, A. Obbadi, S. Sahnoun, Control of PMSG wind electrical system in network context and during the MPP tracking process, *Int. J. Syst. Control Commun.* 11 (2) (2020) 200–225, <https://doi.org/10.1504/IJSCC.2020.106578>.
- [45] R. Gianto, Steady-state model of DFIG-based wind power plant for load flow analysis, *IET Renew. Power Gener.* 15 (8) (2021) 1724–1735, <https://doi.org/10.1049/rpg2.12141>.
- [46] R. Shankar, T. Sengolrajan, K. Mohanraj, B. Balraj, Integration of wind and solar farms in a doubly fed induction generator using hybrid GA-ANN controllers, *Electr. Power Syst. Res.* 213 (2022), 108764, <https://doi.org/10.1016/j.epr.2022.108764>, August.
- [47] J. Baran, A. Jaderko, An MPPT control of a pmsg-based wecs with disturbance compensation and wind speed estimation, *Energies* 13 (23) (2020) 6344, <https://doi.org/10.3390/en13236344>.
- [48] E. Chetouani, Y. Errami, A. Obbadi, S. Sahnoun, Maximum power point tracking design using particle swarm optimization algorithm for wind energy conversion system connected to the grid, *Renew. Energy Syst. Model. Optim. Control* (2013) 445–470, <https://doi.org/10.1016/B978-0-12-820004-9.00009-7>, 2021.
- [49] A. Tounsi, H. Abid, Generator and grid side converter control for wind energy conversion system, *Int. J. Power Electron. Drive Syst.* 12 (3) (2021) 1832–1844, <https://doi.org/10.11591/ijpeds.v12.i3.pp1832-1844>.
- [50] X. Zhou, Y. Zhou, Y. Ma, L. Yang, X. Yang, B. Zhang, DC bus voltage control of grid-side converter in permanent magnet synchronous generator based on improved second-order linear active disturbance rejection control, *Energies* 13 (18) (2020), <https://doi.org/10.3390/en13184592>.
- [51] C. Chen, Self-tuning PID control of induction motor speed control system based on diagonal recurrent neural network, *Int. J. Control Autom.* 8 (10) (2015) 321–334, <https://doi.org/10.14257/ijca.2015.8.10.30>.
- [52] H. Hu, T. Wang, H. Wang, C. Wang, Q-learning optimized diagonal recurrent neural network control strategy for brushless direct current motors, *Adv. Mech. Eng.* 12 (9) (2020) 1–11, <https://doi.org/10.1177/1687814020958221>.
- [53] T. Varshney, S. Sheel, A new online tuning approach for pid control of multivariable systems using diagonal recurrent neural network, in: *Proc. - 2011 IEEE Int. Conf. Control Syst. Comput. Eng. ICCSCE*, 2011, pp. 317–320, <https://doi.org/10.1109/ICCSCE.2011.6190544>, April2011.